https://doi.org/10.5194/egusphere-2026-2170
Preprint. Discussion started: 19 June 2026

From sub-daily to multi-year: permafrost ground surface deformation processes revealed by collocated multi-sensor observations at a supersite on the Tibetan Plateau

Lingxiao Wang[1], Wei Wan[2,*], Lin Zhao[1,*], Wei Chen[1], Chong Wang[1], Shibo Liu[1], Guangyue Liu[3], Yuanwei Wang[1], Junhao Qu[1], Defu Zou[3], Erji Du[3], Guojie Hu[3], Yao Xiao[3], Yonghua Zhao[3], Minxuan Xiao[1]

[1] School of Geographical Sciences, Nanjing University of Information Science & Technology (NUIST), Nanjing 210044, China.
[2] Institute of Remote Sensing and GIS, School of Earth and Space Sciences, Peking University, Beijing, China.
[3] Cryosphere Research Station on the Qinghai-Tibet Plateau, State Key Laboratory of Cryospheric Science and Frozen Soil Engineering, Northwest Institute of Eco-Environment and Resources, Chinese Academy of Sciences, Lanzhou 730000, China.

Correspondence to: Lin Zhao (lzhao@nuist.edu.cn) and Wei Wan (w.wan@pku.edu.cn)

Abstract. Ground surface deformation in permafrost terrain provides critical information on heat and mass transfer during soil freezing and thawing, and serves as a key indicator of permafrost dynamics. However, continuous observations at minute-scale resolution remain extremely rare, sub-daily deformation processes are still poorly documented, and the consistency among remote sensing, contact, and non-contact in situ measurements has not been systematically evaluated. To address these gaps, we established an intensively instrumented permafrost deformation monitoring supersite in an alpine meadow on the central Tibetan Plateau. Ground surface deformation was measured using collocated linear variable differential transformer (LVDT) sensors, ultrasonic ranging, GNSS interferometric reflectometry (GNSS-IR), and Sentinel-1 SBAS-InSAR, together with multi-layer soil temperature and moisture observations. Automated LVDT-based observations provided continuous 5 min deformation records with sub-millimetre precision from 2022 to 2026, thereby resolving, for the first time, sub-daily deformation processes across different freeze–thaw stages. Results show that active layer thaw settlement commonly develops in a stepwise manner within a day, whereas late-thaw-season subsidence associated with excess ground ice melt is more continuous, reflecting sustained drainage and compression. This process also gives rise to a breakpoint-style acceleration in subsidence during the late thaw season. The sub-daily record further clarifies the origin of short-lived late-winter heave events, which are most consistent with infiltration and rapid refreezing of liquid water in shallow soil. The four deformation datasets show broadly consistent temporal patterns. LVDT and InSAR agree closely ($r = 0.91$), whereas GNSS-IR and ultrasonic ranging show even stronger agreement ($r = 0.96$). InSAR maintains strong agreement with the other observation methods in both the freezing and thawing seasons, with correlation coefficients consistently exceeding 0.86. GNSS-IR and ultrasonic ranging are more affected by snow and vegetation and require substantial filtering, making them more suitable for seasonal- to multi-year monitoring than for resolving subtle sub-daily

https://doi.org/10.5194/egusphere-2026-2170
Preprint. Discussion started: 19 June 2026

signals. At our site, settlement during the active layer thaw stage is strongly correlated with the square root of thawing degree days ($\sqrt{TDD}$) across all four thaw seasons ($R^2 > 0.96$), and ice–water phase change within the active layer can explain more than 78 % of the observed seasonal deformation. These results provide a valuable observational benchmark for permafrost deformation from sub-daily to multi-year timescales and support improved process-based modelling and interpretation of GNSS-IR and InSAR observations in permafrost regions.

Keywords: ground surface deformation, permafrost, in-situ monitoring, sub-daily process, GNSS-IR, InSAR

1 Introduction

Ground surface deformation in permafrost terrain is a key periglacial expression of coupled thermal, hydrological, and mechanical processes within the active layer and underlying permafrost. At diurnal to seasonal timescales, deformation is mainly governed by frost heave and thaw subsidence associated with freeze–thaw cycling (J. Chen et al., 2020; Du et al., 2025; Smith, 1987). At multi-annual to decadal timescales, deformation reflects changes in ground ice storages: thaw of ice-rich permafrost and subsequent consolidation can produce persistent subsidence, whereas ground ice aggradation may lead to long-term surface uplift (Kokelj et al., 2007; Mackay & Burn, 2002; O'Neill & Burn, 2012; Shiklomanov et al., 2013; Streletskiy et al., 2025). Ground deformation information is a sensitive observable for diagnosing permafrost responses to climate change, and useful for assessing associated hazards to infrastructure and slopes, as well as hydrological and ecological impacts linked to ground ice changes (Hjort et al., 2022; Kokelj et al., 2021; Nitzbon et al., 2020) as it integrates changes in temperature, phase state, water redistribution, and ground ice content.

Continuous in situ deformation records are therefore essential, yet long, multi-annual records that capture complete freeze–thaw cycles remain rare in both the pan-Arctic and on the Tibetan Plateau permafrost regions. To our knowledge, work of (Gruber, 2020) remains one of the very few studies to report and analyse continuous ground surface deformation measurements at hourly resolution over a period exceeding two years, based on observations from Yellowknife, Northwest Territories, Canada. Traditional approaches, including geodetic levelling (S. Liu et al., 2022; Mackay & Burn, 2002), differential GNSS surveys (Little et al., 2003; Streletskiy et al., 2016), and thaw tubes (Antonova et al., 2018; O'Neill et al., 2019; Short et al., 2014), are typically based on repeated field visits (Kokelj et al., 2007) and therefore lack the temporal continuity needed to resolve process-level deformation dynamics. To address this gap, automated ground-based monitoring systems have been increasingly used. Among them, contact-based linear variable differential transformer (LVDT) sensors are particularly well suited to harsh permafrost environments because of their high precision and mechanical robustness (Harris et al., 2007; Matsumoto et al., 2010).Tilt-arm systems, which are also in contact way, have been used in permafrost deformation monitoring too, including in the Yellowknife, Northwest Territories, Canada (Gruber, 2020) and in the northeastern region of the Qinghai-Tibet Plateau (Fan et al., 2025). By contrast, sonic ranging represents a non-contact approach. Originally developed for snow depth or water level measurements, they can also be used to monitor ground

https://doi.org/10.5194/egusphere-2026-2170
Preprint. Discussion started: 19 June 2026

surface elevation change when mounted on stable monuments, although they remain sensitive to snow and vegetation and are therefore more commonly applied during snow-free periods and over sparsely vegetated terrain (Overduin & Kane, 2006). Global Navigation Satellite System Interferometric Reflectometry (GNSS-IR) has recently emerged as another promising technique, providing daily, and under suitable conditions sub-daily, deformation estimates over a footprint (from a few meters to several tens of meters) larger than that of point sensors. However, applications of GNSS-IR to permafrost remain limited because of strict site requirements and the scarcity of suitable stations (J. Zhang et al., 2020). To date, most GNSS-IR studies of permafrost deformation have focused on a small number of well-instrumented sites, such as SG27 at Barrow (Hu et al., 2022; L. Liu & Larson, 2018; Tu et al., 2025). On the Tibetan Plateau, applications remain especially scarce and, to our knowledge, are limited to work of (J. Zhang et al., 2021) in the northern plateau and our previous studies in the plateau interior (W. Chen et al., 2025).

At broader scales and spatial monitoring, InSAR has become a primary tool for mapping seasonal and long-term permafrost deformation with millimetre- to centimetre-level precision (Z. Zhang et al., 2022; Zwieback, Liu, et al., 2024). However, revisit intervals and decorrelation over wet or vegetated terrain strongly limit its ability to resolve high-frequency deformation processes and to capture process-level details. These observational limitations are particularly important because interpretation of permafrost deformation increasingly depends on temporal resolution. Recent InSAR-based studies have suggested that, once the thaw front penetrates into the upper ice-rich permafrost in the late thaw season, melt of excess ground ice can accelerate subsidence beyond that associated with active layer thaw (Wendt et al., 2026; Zwieback & Meyer, 2021), and that such late-season subsidence may be used to identify ice-rich permafrost and map ground ice content (Zwieback et al., 2025; Zwieback, Iwahana, et al., 2024). However, this remains untested by continuous in-situ deformation records with sufficient temporal resolution to directly resolve the underlying process. More broadly, the lack of co-located multi-sensor observations with concurrent hydrothermal measurements has limited the evaluation of the consistency, uncertainty, and physical significance of deformation signals obtained from different monitoring approaches. At the same time, recent advances in Earth system modelling of permafrost change and ground surface deformation have created an urgent need for accurate, continuous, and high-temporal-resolution deformation observations (Aga et al., 2023). This is especially true for sub-daily deformation processes, which remain poorly documented in permafrost terrain and are still not well understood from direct observations.

To address these gaps, we established an intensively instrumented permafrost-deformation supersite in the central Tibetan Plateau, where a ground-based monitoring system integrating LVDT measurements, ultrasonic ranging, GNSS-IR, and multi-layer hydrothermal observations has been in operation since 2021. These in situ observations were further complemented by deformation time series derived from Sentinel-1 SBAS-InSAR. Using the above dataset spanning 2022–2026, we (i) describe the design and performance of a fully automated, high-temporal-resolution in-situ ground surface deformation monitoring system; (ii) reveal sub-daily deformation processes during different freeze–thaw stages by

https://doi.org/10.5194/egusphere-2026-2170
Preprint. Discussion started: 19 June 2026

integrating multi-layer soil temperature and moisture observations; (iii) intercompare deformation time series derived from LVDT, ultrasonic ranging, GNSS-IR, and InSAR, and quantify their agreements and discrepancies; and (iv) identify deformation signatures associated with deep thaw and excess ground ice melt in deformation time series.

2 Study area and measurement sites

The monitoring station (91.29° E, 32.88° N; 4990 m a.s.l.) is located in the interior of the Tibetan Plateau (Figure 1a), in the upper reaches of the Zhajiazangbu River (Za'gya Zangbo) within the Selin Co (lake) watershed. Selin Co is one of the most rapidly expanding lakes on the Tibetan Plateau in recent decades, and ground ice meltwater has been estimated to contribute approximately 12 % of the lake expansion volume (Wang et al., 2022).

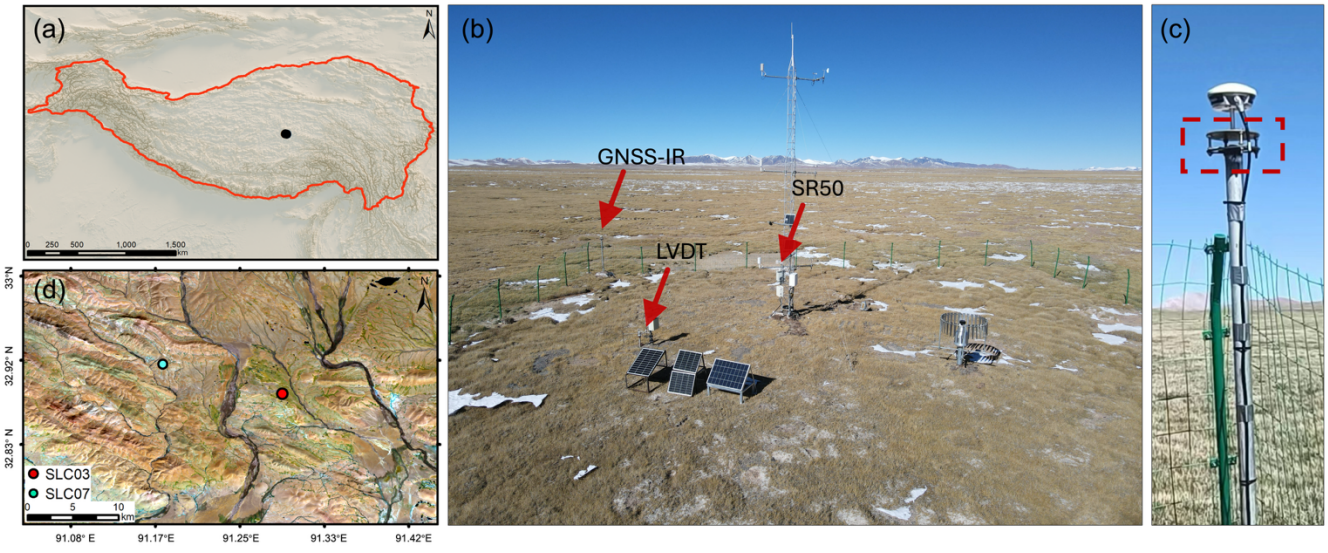

Figure 1. Study area and measurements. (a) Location of the study area on the Tibetan Plateau. (b) Instrument layout at the meteorological and permafrost monitoring station, with the surrounding alpine swamp meadow. (c) GNSS antenna and its monument. (d) Locations of the two automated LVDT-based in situ ground surface deformation monitoring sites.

The region is characterized by a cold, semi-arid plateau climate influenced by the Asian monsoon. Based on observations from 2022–2024, the mean annual air temperature is -4.6 °C, with January as the coldest month (-17.6 °C) and August as the warmest month (6.9 °C). Annual precipitation ranges from 463 to 551 mm, with more than 50 % falling between June and September. The year with the highest precipitation was 2023 (551.1 mm), followed by 2022 (466.9 mm) and 2024 (462.9 mm). Winters are cold, dry, and windy, resulting in thin and short-lived snow cover. Mean wind speed at 2 m height is 4.7 m/s, and mean incoming shortwave radiation is 225.69 W/m^2. Borehole drilling and field observations indicate that the area is underlain by ice-rich permafrost, with an active layer thickness of (ALT) of ~3 m. The permafrost is relatively warm and

https://doi.org/10.5194/egusphere-2026-2170
Preprint. Discussion started: 19 June 2026

has been undergoing rapid degradation; borehole measurements show a ground temperature of approximately -2 °C at 10 m depth.

3 Methods and datasets

The supersite combines collocated LVDT-based measurements, ultrasonic ranging, and GNSS-IR observations of ground surface elevation change, complemented by Sentinel-1 InSAR over the surrounding region. Borehole drilling conducted during the Second Tibetan Plateau Scientific Expedition in November 2019 laid the foundation for subsequent permafrost observations. In November 2021, a meteorological and permafrost monitoring station was installed, equipped with a GNSS receiver (Trimble NetR9), an automated ground surface deformation monitoring system, and active-layer hydrothermal sensors initially spanning depths of 5–50 cm. On 10 August 2022, the soil sensor array was extended to 240 cm and relocated approximately 10 m from its original position. The LVDT system provides 5 min in situ displacement records that resolve sub-daily variability and allow detailed characterization of diurnal deformation processes. Ultrasonic ranging, although sensitive to snow cover and vegetation, offers a useful non-contact complement to point-based displacement measurements and supports cross-validation of deformation signals. Table 1summarizes the observational footprint and temporal sampling interval of the in-situ deformation monitoring methods used in this study.

Table 1. Information on in-situ LVDT-based, ultrasonic ranging, and GNSS-IR monitoring of ground deformation.

Observation	Observation footprint (diameter)	Observation interval	Time step used for analysis
LVDT-based measurement	8 cm	5 min	5 min and 1 d
Ultrasonic ranging	~1 m	10 min	1 d
GNSS-IR	~50 m	1 s	1 d

To capture spatial variability, an additional LVDT-based automated deformation monitoring system was deployed at a second borehole site (SLC07), located 10.6 km northwest of the main station (supersite SLC03). Surface conditions differ between the two sites: SLC03 is situated in alpine swamp meadow (Figure 1b), whereas SLC07 is located in degraded alpine meadow with very sparse vegetation. The main station has cellular coverage and transmits data in near real time, whereas SLC07 lacks network connectivity; its data are stored locally and retrieved during annual field visits. Although the sensors were installed in November 2021, excavation and installation disturbed the ground surface at SLC03, we therefore only analysed data from SLC03 after June 2022. In contrast, no excavation was conducted at SLC07, and thus the deformation record from that site is analysed from November 2021 onward.

https://doi.org/10.5194/egusphere-2026-2170
Preprint. Discussion started: 19 June 2026

3.1 In situ automated ground surface deformation monitoring system with LVDT sensor

The developed automated deformation monitoring system consists of a LVDT displacement sensor, a data transmission unit (DTU) for remote telemetry or datalogger, and a solar-powered energy supply, shown in Figure 2. The LVDT sensor used in this study had a measurement range of 150 mm, a linearity error of ≤ 0.25 % of full scale, and a recording resolution of 0.01 mm. Each LVDT sensor was installed adjacent to a steel reference rod anchored deeply into ground (30 m), which served as a stable benchmark. The lower end of the sensor was connected to a perforated footplate resting on the ground surface. The footplate was 8 cm in diameter and moved vertically with the ground surface as it heaved or subsided. Multiple holes in the footplate allowed water and air exchange with the underlying soil while minimizing disturbance to surface energy and moisture fluxes (Figure 2c). Because the plate remained in direct contact with the ground surface beneath snow and vegetation (Figure 2d), the measurements were less affected by changing surface cover than those from non-contact methods. The LVDT sensor converts the relative motion of a ferromagnetic core, driven by the vertical movement of the footplate as the ground surface heaves or subsides, into a digital signal that is transmitted via Modbus RTU over an RS-485 interface. At sites with network coverage, a data transfer unit (DTU) uploads the measurements to a remote server through the mobile network; otherwise, the data are stored locally by a datalogger.

Before November 2023, the power supply at SLC03 was insufficient for stable night-time operation, so daily values were calculated from daytime observations only (10:00–18:00 local time). After a power upgrade in November 2023, daily values were computed from the full 24 h record. At SLC07, daily values were consistently derived from daytime observations because the power-constrained configuration remained unchanged. Potential errors related to thermal expansion and contraction of the sensor assembly were not explicitly corrected, but no systematic deformation signal covarying with temperature was evident, which will be illustrated and stated in section 5.1.

https://doi.org/10.5194/egusphere-2026-2170
Preprint. Discussion started: 19 June 2026

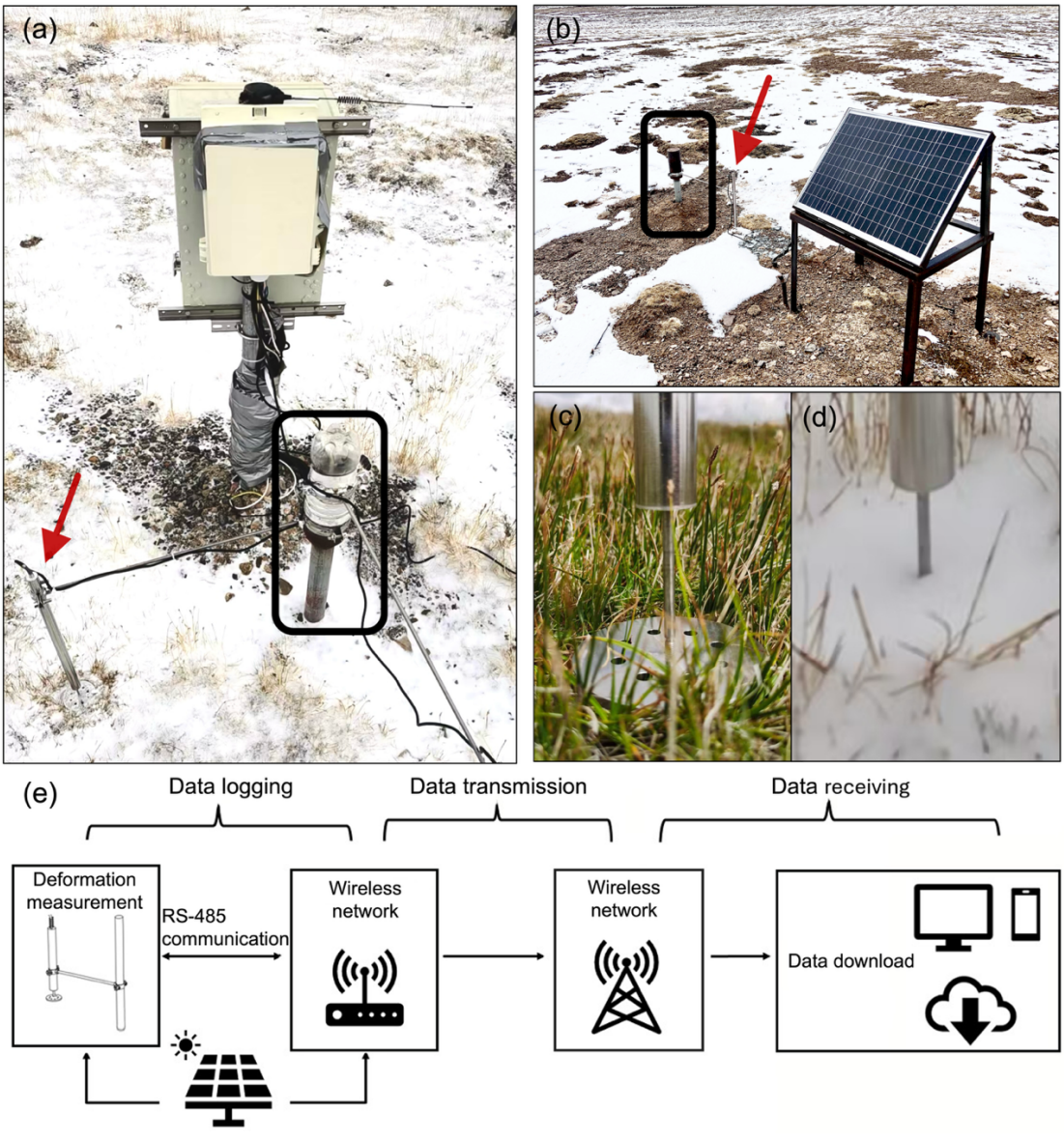

Figure 2. (a)–(b) Field photographs of the LVDT-based automated in situ ground surface deformation monitoring apparatus installed at the two sites. The black box in the (a)(b) marks the borehole steel pipe used as the reference for deformation measurements. The red arrow marks the LVDT sensor. The LVDT sensor was fixed to a stable steel rod anchored in permafrost and measured the vertical motion of a perforated footplate resting on the ground surface. (c)–(d) Enlarged views of the sensor footplate in summer and winter. (e) Schematic of the sensor–logger system, including the LVDT, DTU/datalogger, and solar power supply.

https://doi.org/10.5194/egusphere-2026-2170
Preprint. Discussion started: 19 June 2026

3.2 Ultrasonic ranging measurements

An ultrasonic ranging sensor (Sonic Ranger SR50A, Campbell Scientific) was mounted on a steel meteorological tower at 2 m above the ground (Figure 1b), with the tower foundation anchored 6 m into the ground. It emits ultrasonic pulses and determines sensor–surface distance from the two-way travel time of the returned echo using a temperature-corrected sound speed. The sensor records the nearest target within a conical field of view of 30°. The SR50A has a measurement resolution of 0.25 mm and accuracy of ± 1 cm.

To reduce sporadic upward spikes, such as those caused by snow or vegetation, while preserving the slowly varying ground-deformation signal, we applied a despiking and smoothing procedure to the ultrasonic-ranging time series. First, a centered 7 d rolling median was used to define the local baseline, and deviations were evaluated using a rolling median absolute deviation (MAD). Points showing upward excursions greater than three times the local MAD ($|\,\text{data} - \text{median}\,| > K \cdot 1.4826 \cdot \text{MAD}$, with $K = 3$) were flagged as outliers and removed. The despiked series was then smoothed using a centered 5 d median filter followed by a centered 11 d moving-average filter.

3.3 GNSS-IR receiver setting and data processing

The GNSS antenna was mounted on a custom steel pipe 2.13 m above the ground and anchored 6 m into the ground. A levelling base was used to ensure a horizontal mount (Figure 1c). Based on the first Fresnel zone corresponding to a 5° elevation cutoff (Larson & Nievinski, 2013), the effective GNSS-IR footprint is an elongated area centered approximately 24 m from the antenna nadir.

GNSS-IR infers surface elevation changes from interference between direct and ground-reflected GNSS signals recorded in signal-to-noise ratio (SNR) observations. The dominant frequency component f (Hz) can be extracted from the SNR using Lomb-Scargle Periodogram (LSP) analysis which can be expressed as:

$$SNR = A(e)\,sin(2\pi f\,sin\,e + \phi(e)) \quad (1)$$

Where $A(e)$ and $\phi(e)$ represent the oscillation amplitude and phase offset varying with satellite elevation angle e (degrees). Based the relationship between reflector height and dominant frequency component $f = 2h / \lambda$, the reflector height h can be determined. h (meters) is the reflector height denoting the distance of ground surface relative to receiver, λ (meters) is the GNSS signal wavelength.

We used GPS, GLONASS, and BeiDou observations recorded by a Trimble NetR9 receiver. RINEX files were pre-processed with GFZRNX software to generate standardized daily files at a 30 s sampling interval. GNSS-IR reflector heights (RH) were retrieved using GiRsnow software with settings of satellite elevation angle of 5–25° and azimuth of 0–360°. A

https://doi.org/10.5194/egusphere-2026-2170
Preprint. Discussion started: 19 June 2026

more detailed description of the configuration and data processing can be found in our previous study (W. Chen et al., 2025). Two post-processing steps were applied to the derived RH series. First, track-level RH estimates were aggregated to daily values after robust outlier screening using a MAD criterion ($|\ RH - median\ | > K \cdot 1.4826 \cdot MAD$, with K = 3). Second, the daily series was screened for isolated spikes using a local-window filter: values differing from surrounding observations by more than 1 cm were replaced by a local linear least-squares estimate based on neighbouring valid observations. This procedure corrects only locally inconsistent points while preserving broader seasonal and interannual variability.

3.4 Sentinel-1 SBAS-InSAR ground surface deformation monitoring

Sentinel-1 SBAS-InSAR processing was applied to derive ground surface deformation in the area surrounding the in-situ monitoring site. The Sentinel-1 SLC data were acquired in interferometric wide-swath mode on the ascending track (Path 41) from 5 August 2017 to 15 November 2025, with 250 acquisition dates in total. Processing was performed using ISCE2 and MintPy software. Interferograms were generated by pairing each SAR acquisition with its two subsequent images ($t - t + 1$ and $t - t + 2$). Surface deformation was estimated relative to a reference point located near SLC03 on a small hill (Figure 3a, 3b), which maintained coherence values above 0.99 in all interferograms. During processing, 10 looks in range and 2 looks in azimuth were applied to reduce noise and produce an approximately square grid (finally geocoded to 40 m grid). Differential phases were unwrapped using the SNAPHU minimum cost flow algorithm (C. W. Chen & Zebker, 2002), and the interferogram network was inverted into a deformation time series using a weighted least-squares approach. After inversion, phase deramping, and topographic residual correction were applied. A temporal moving-window filter (window size = 3) was further used to smooth the deformation time series. More details of the SBAS-InSAR workflow are given in our previous study (Wang et al., 2022). Because the terrain is relatively flat and deformation is expected to be dominated by freeze-thaw-related vertical motion, line-of-sight (LOS) deformation was converted to vertical displacement by dividing by the cosine of the incidence angle, assuming negligible horizontal motion.

3.5 Meteorological and active layer hydrothermal monitoring

Meteorological and active layer hydrothermal observations were used to support interpretation of ground deformation processes, including 2 m air temperature, precipitation, soil temperature (ST), and soil volumetric water content (VWC). Air temperature was measured with a Vaisala HMP155 sensor (accuracy 0.18–0.26 °C over the temperature range relevant to the study area). Precipitation was recorded by a Geonor T-200B gauge (full-scale error 0–0.04 %). Soil temperature and moisture were monitored using Campbell Scientific SM926 sensors (± 0.3 °C and ± 3 % vol, respectively). Soil temperature and moisture were monitored from 0.05 to 2.4 m depth at 10 min intervals and then aggregated to daily values. Daily air temperature was used to calculate accumulated degree days of thawing (DDT) and freezing (DDF). Thawing and freezing

https://doi.org/10.5194/egusphere-2026-2170
Preprint. Discussion started: 19 June 2026

onset were defined as the first day when the daily mean air temperature remained above or below 0 °C for seven consecutive days.

4 Results

4.1 Multi-sensor observations of ground surface deformation

4.1.1 Ground surface deformation from Sentinel-1 InSAR

In the study area, the land surface is covered by alpine meadow in summer, while winter snow cover is generally thin and short-lived. As a result, interferometric pairs acquired within intervals of up to one month generally retain relatively high coherence throughout the year. The coherence distribution of the interferometric pairs used in this study is presented in Appendix Figure A1. The reference point showed a very high mean coherence of 0.99 across all interferometric pairs and was located near the monitoring sites, approximately 5 km from SLC03 and 11 km from SLC07. Given this spatial proximity, subtracting the deformation at the reference point helped reduce the influence of common atmospheric artefacts and potential regional crustal motion in the deformation time series at the monitoring sites.

The InSAR-derived deformation results provide a regional-scale context for interpreting the point-scale ground observations. Combined with Figure 1d, the spatial pattern shown in Figure 3a–b reveals that deformation in the non-permafrost floodplain and on small hills was markedly weaker than that in the alpine swamp meadow and alpine meadow permafrost areas. Figure 3c–d shows the Sentinel-1 InSAR-derived deformation time series at SLC03 from August 2017 to November 2025. The time series exhibits a clear seasonal cycle superimposed on a persistent long-term subsidence trend. Each year is characterized by winter freeze uplift and summer thaw subsidence, with seasonal deformation magnitude generally on the order of several centimetres. By late 2025, cumulative vertical subsidence reached ~140 mm relative to the beginning of the series. The subsidence trend over the full observation period is 14.89 mm/yr, whereas the subsidence trend since November 2021 is severer, at 19.18 mm/yr, indicating enhanced surface lowering during the recent monitoring period.

https://doi.org/10.5194/egusphere-2026-2170
Preprint. Discussion started: 19 June 2026

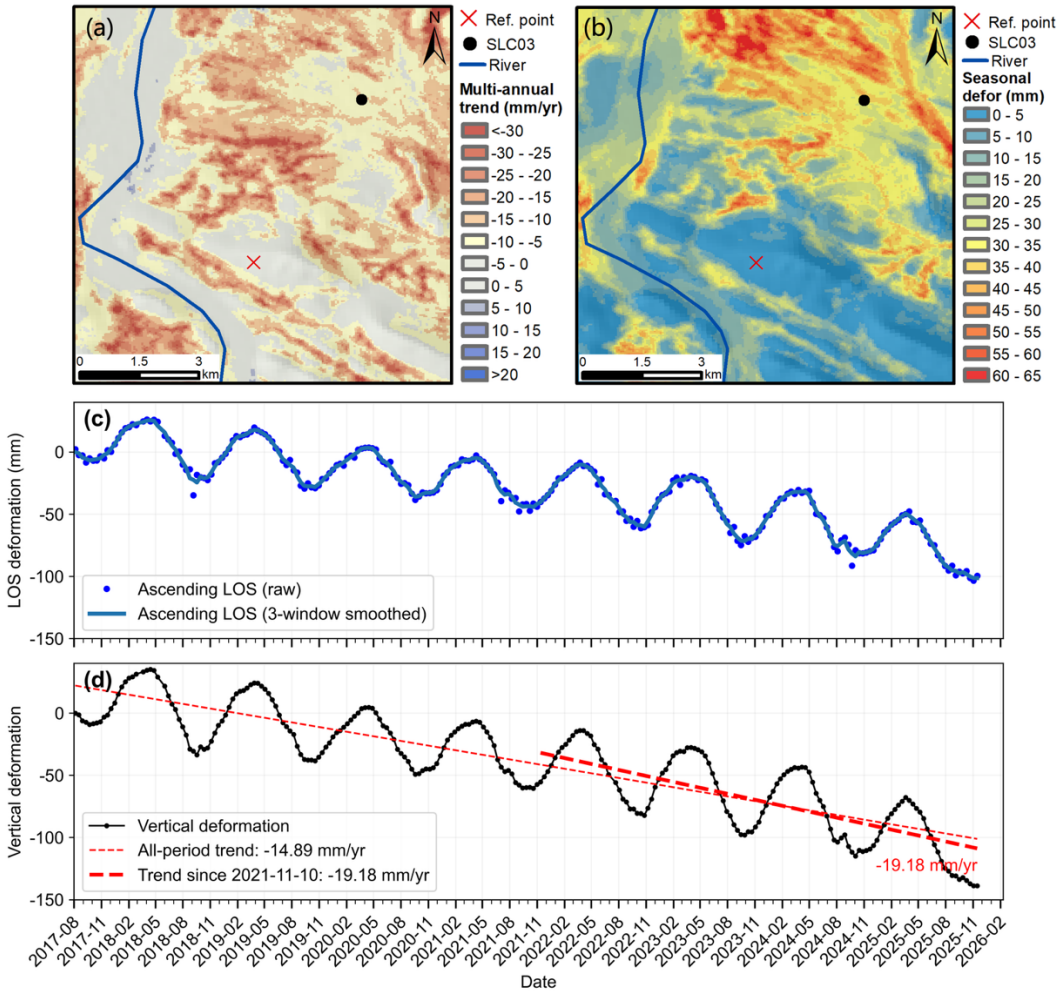

Figure 3. Sentinel-1 InSAR deformation. (a, b) Spatial distribution of seasonal deformation and long-term deformation trend in the line-of-sight (LOS) direction around the supersite. (c) LOS deformation time series at SLC03 site. (d) Vertical deformation time series converted from LOS deformation, together with the linear trend.

4.1.2 Ground surface deformation from LVDT-based measurements

The in situ LVDT measurements reveal repeated frost-heave and thaw-settlement cycles at both SLC03 and SLC07, while also highlighting pronounced interannual and inter-site differences in seasonal amplitude, timing, and long-term trend, shown in Figure 4. SLC03 exhibits markedly larger seasonal deformation and a stronger long-term downward trend than SLC07. At SLC03, both the seasonal maxima and minima shift progressively downward from year to year, indicating persistent subsidence. In contrast, at SLC07, seasonal minima shift progressively downward from year to year, but the winter maxima do not show a continuous year-to-year downward shift, indicating weaker cumulative lowering and a less

https://doi.org/10.5194/egusphere-2026-2170
Preprint. Discussion started: 19 June 2026

pronounced long-term trend. At the SLC07 site, seasonal deformation during the 2023–2024 freeze–thaw cycle was markedly greater than in the preceding two years. This enhancement was likely associated with exceptionally high summer precipitation in 2023, which may have increased active-layer water content prior to freezing. By contrast, no similarly anomalous increase in seasonal deformation was observed at the SLC03 site during the 2023–2024 freeze–thaw cycle. At SLC03, the thaw-season minima deepen from about -78 mm in 2022 to nearly -96 mm in 2023 and to about -130 mm in 2025. At SLC07, the thaw-season minima deepen from about -39 mm in 2022 to about -58 mm in 2024.

Differences between the two sites are also evident in the timing and shape of seasonal transitions. Frost heave begins about half a month earlier at SLC07 than at SLC03. At SLC03, the onset of frost heave generally occurs in early November, lagging behind the onset of surface freezing in October. At SLC07, the deformation curve becomes relatively flat after January and shows little additional heave until April. By contrast, SLC03 continues to exhibit slow late-winter uplift. During thaw, settlement also begins earlier at SLC07, whereas at SLC03 the onset of rapid settlement is delayed until June in some years. Maximum thaw settlement at SLC07 occurs much earlier, especially in 2023 and 2024, with subsidence becoming nearly stable after August; by contrast, in 2022 a distinct thaw-season breakpoint is evident around 20 July. At SLC03, a late-thaw-season breakpoint followed by accelerated subsidence is also observed in 2022, 2024, and 2025, and is particularly pronounced in 2024.

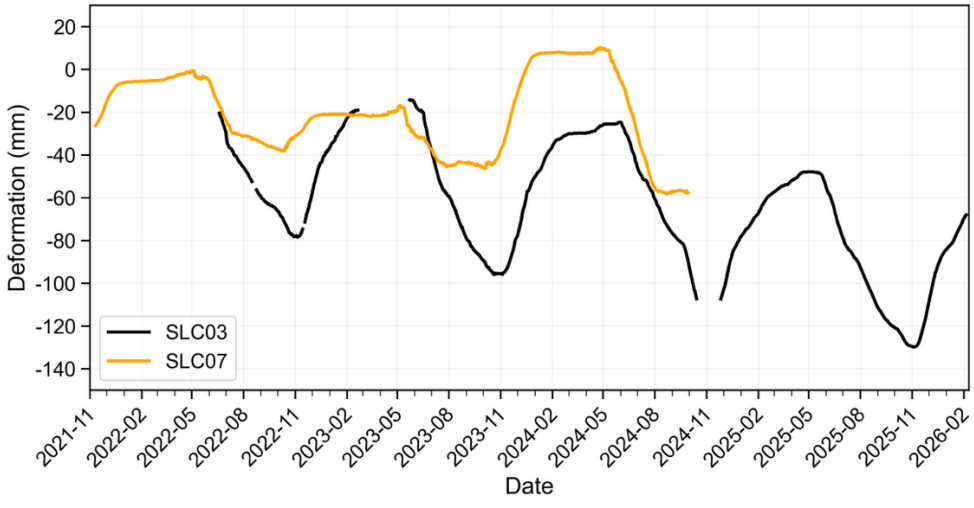

Figure 4. Multi-year ground surface deformation time series from in situ LVDT-based measurements at SLC03 and SLC07. Data gaps during several periods were primarily caused by power-supply failures. In late October 2024, the LVDT record was further interrupted because ground subsidence exceeded the sensor's measurement range. Measurements resumed in December 2024, when frost heave raised the ground surface back within the sensor's measurement range.

https://doi.org/10.5194/egusphere-2026-2170
Preprint. Discussion started: 19 June 2026

4.1.3 Ground surface deformation from ultrasonic ranging

The ultrasonic ranging record shows pronounced long-term surface lowering superimposed on repeated seasonal deformation cycles (Figure 5). In the raw series, numerous short-lived positive excursions occur throughout the record. These spikes are mainly associated with snow. On the Tibetan Plateau, snow cover is generally thin and short lived, and under strong radiation it often melts or sublimates within one or a few days. After despiking and smoothing, the resulting series suppresses most of the short-term excursions and shows a much clearer seasonal signal and a persistent multi-year subsidence trend. However, it should be also noted that when snow cover persists for an extended period, the snow signal cannot be readily removed by filtering and may become mixed with the ground deformation signal, as observed at the end of October in 2022 and 2023.

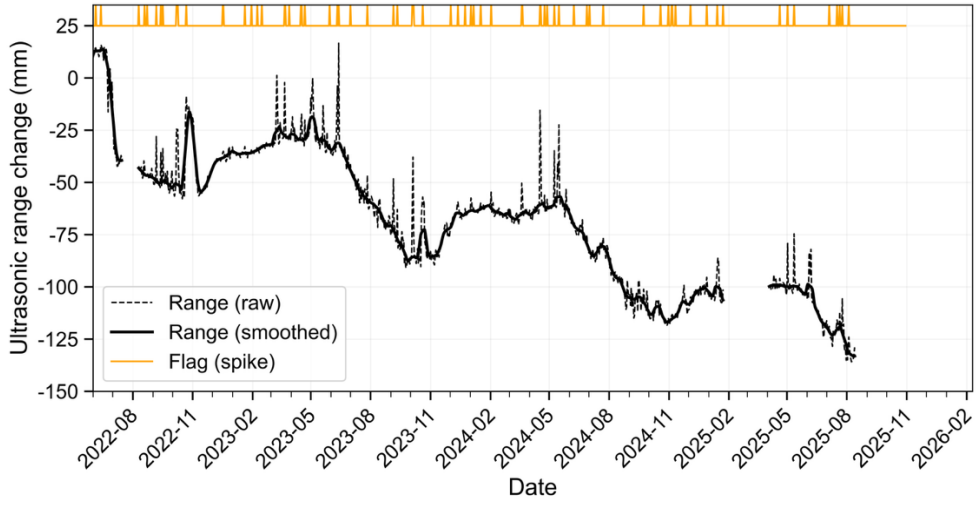

Figure 5. Raw and post-processed ultrasonic ranging measurements. Orange markers indicate observations flagged as spikes, corresponding to short-lived upward excursions (mainly caused by snow) in the raw series.

4.1.4 Ground surface deformation from GNSS-IR

The raw GNSS-IR time series exhibits substantial scatter and occasional large excursions, particularly during the cold season and transition periods, reflecting the sensitivity of reflector height retrievals to changing surface and observation conditions (Figure 6). After smoothing, the deformation process becomes much clearer and shows a coherent pattern of seasonal uplift during the freezing season and thaw-season subsidence, together with a persistent downward shift through time. From June 2022 to September 2025, the smoothed GNSS-IR series indicates an overall cumulative lowering of more than 110 mm.

https://doi.org/10.5194/egusphere-2026-2170
Preprint. Discussion started: 19 June 2026

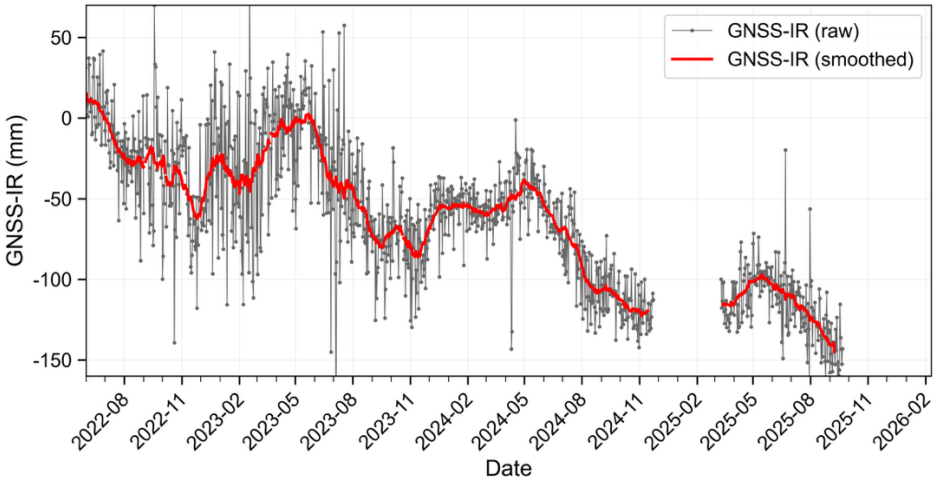

Figure 6. Ground surface deformation derived from GNSS-IR. The receiver experienced a power failure in December 2024 and was restored in March 2025, resulting in a data gap during this period.

315

4.2 Intercomparison of multi-sensor ground surface deformation records

To compare similarities and differences among the four observation systems, the deformation records were analysed together in the context of freeze–thaw stages inferred from active layer hydrothermal monitoring. Each freeze–thaw cycle was divided into four stages: (i) active layer thawing above 220 cm (AT), (ii) late thawing below 220 cm (LT), (iii) active layer
320 freezing above 220 cm (AF), and (iv) Late-winter freezing (LF). Because the soil temperature and moisture observations at 240 cm depth contain large data gaps, the 220 cm depth was used as the indicator of thaw or freeze progression near the base of the active layer. Definitions of these stages are summarized in Table 2. Figure 7 shows the four deformation records (LVDT, GNSS-IR, ultrasonic ranging, and InSAR) together with the corresponding meteorological and soil hydrothermal profiles at SLC03. Despite substantial differences in sensor footprint and noise level, all methods capture the seasonal
325 freeze–thaw cycle and the progressive subsiding of the ground surface from 2022 to 2025. The records also indicate that some subsidence continues during the early part of AF stage, implying that deep thaw settlement still persist after shallow soil has begun to refreeze.

330

https://doi.org/10.5194/egusphere-2026-2170
Preprint. Discussion started: 19 June 2026

Table 2. Definitions and characteristics of different freeze–thaw stages.

Freeze/thaw stage	Criteria for identifying different freeze–thaw stages	Period			Thermal accumulation (°C·d)
		Stage	Date	Duration (days)	
Active layer thawing (AT)	This period begins when the daily mean air temperature remains above 0 °C for seven consecutive days.	AT-2022	20220524–20220812	81	493.2
		AT-2023	20230528–20230921	117	557.3
		AT-2024	20240519–20240908	113	637.8
		AT-2025	20250524–20250820	89	482.6
Late-summer thawing (LT)	Following AT, LT represents thawing of soil layers below 220 cm and is identified by a sharp increase in soil moisture at 220 cm.	LT-2022	20220813–20221012	61	222.1
		LT-2023	20230922–20231010	19	30.7
		LT-2024	20240909–20241010	32	114.5
		LT-2025	20250821–20251010	51	180.3
Active layer freezing (AF)	This period begins when the daily mean air temperature remains below 0 °C for seven consecutive days.	AF-2022–23	20221013–20230208	119	-1498.6
		AF-2023–24	20231011–20240205	118	-1591.7
		AF-2024–25	20241011–20250215	128	-1484.1
		AF-2025–26	20251011–202602		
Late-winter freezing (LF)	Following AF, LF is identified when soil liquid water content at 220 cm shows a sharp decrease and falls below 0.1 m^3/m^3.	LF-2022–23	20230209–20230527	108	-811.0
		LF-2023–24	20240206–20240518	103	-842.7
		LF-2024–25	20250216–20250523	97	-612.8

https://doi.org/10.5194/egusphere-2026-2170
Preprint. Discussion started: 19 June 2026

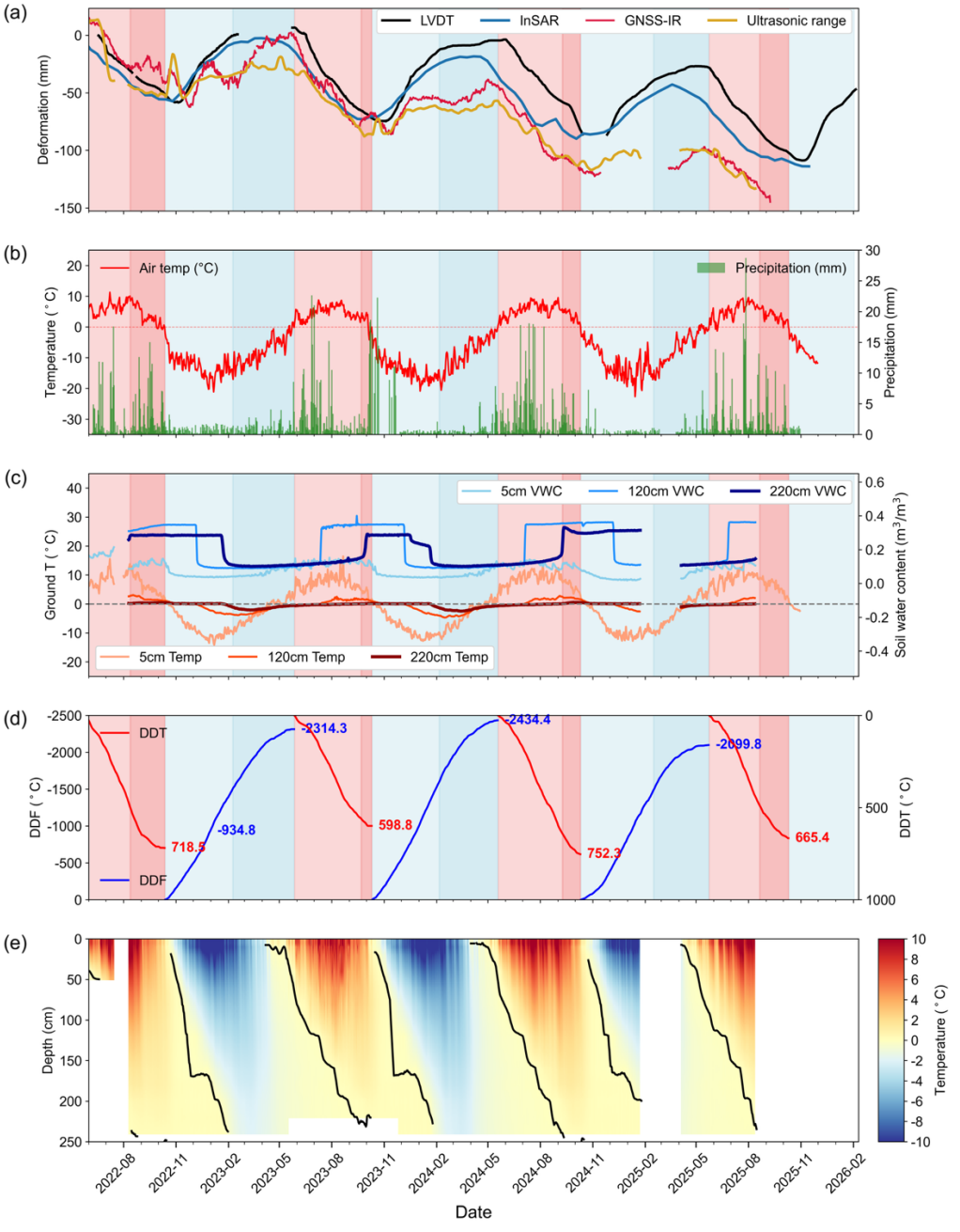

Figure 7. Multi-sensor ground surface deformation and hydrothermal conditions at the SLC03 supersite during 2022–2025. (a) Ground surface deformation time series derived from LVDT, Sentinel-1 SBAS-InSAR, GNSS-IR, and ultrasonic ranging. The deformation time series from different observation methods were referenced to the first day. Shaded blue and red bands indicate freezing and thawing stages, respectively. Light red and red represent AT and LT, and light blue and blue represent AF and LF. (b) Daily air temperature and precipitation. (c) Soil temperature and volumetric water content at 5, 120, and 220 cm depth. (d) degree days of thawing (DDT) and degree days of freezing (DDF). (e) Soil temperature profile; the black line indicates the estimated thaw front based on soil temperature profile.

https://doi.org/10.5194/egusphere-2026-2170
Preprint. Discussion started: 19 June 2026

To further quantify the agreement and discrepancies among the four monitoring records, we extracted the long-term deformation trend and seasonal deformation (peak-to-peak) from each deformation time series using a linear function combined with an intra-annual sinusoidal term. The results of these comparisons are presented in Figure 8. All methods indicate persistent ground surface subsidence at SLC03, with negative multi-annual trends of -16.4 mm/yr for the LVDT record, -19.2 mm/yr for InSAR, -34.6 mm/yr for ultrasonic ranging, and -38.6 mm/yr for GNSS-IR (Figure 8a). The LVDT record shows the largest seasonal deformation (70.8 mm), followed by InSAR (58.4 mm), GNSS-IR (42.8 mm), and ultrasonic ranging (35.8 mm) (Figure 8b). Over the full annual cycle, the LVDT record correlates most strongly with InSAR ($r = 0.91$), whereas its agreement with GNSS-IR and ultrasonic ranging is weaker ($r = 0.62$ and $r = 0.60$, respectively; Figure 8c). During the freeze uplift period (Nov–May), the LVDT and InSAR correlation is 0.92, whereas the LVDT correlations with GNSS-IR and ultrasonic ranging decrease to 0.45 and 0.56, respectively (Figure 8d). During the thaw subsidence period (Jun–Oct), the LVDT and InSAR correlation is 0.9, and the LVDT correlations with GNSS-IR and ultrasonic ranging increase to 0.73 and 0.65, respectively (Figure 8e). GNSS-IR and ultrasonic ranging remain strongly correlated in all periods ($r = 0.95$–0.97). Overall, the four records show a broadly consistent pattern, but LVDT and InSAR are more similar to each other, whereas GNSS-IR and ultrasonic ranging are also more similar to each other.

In the interior Tibetan Plateau, sparse vegetation allows C-band interferometric pairs with temporal baselines of less than one month to maintain high interferometric quality. Although only short-temporal-baseline interferograms were used to derive the deformation time series, the high coherence of individual interferometric pairs and the lack of evident phase unwrapping errors supported a reliable deformation time series inversion, with no clear evidence of error propagation or cumulative bias. As a result, the InSAR-derived deformation in this study agreed closely with the LVDT measurements. The larger GNSS-IR and ultrasonic ranging subsidence trends reflect stronger local thaw disturbance in their observation footprint, confirmed by thermokarst ponds and subsidence developed around their monuments, shown in Appendix Figure A2. In addition, the LVDT reference rod is anchored to 30 m depth, whereas the GNSS-IR and ultrasonic ranging structures are anchored to 6 m depth; possible monument movement, including frost jacking, cannot be fully ruled out and is discussed further in Section 5.1.

https://doi.org/10.5194/egusphere-2026-2170
Preprint. Discussion started: 19 June 2026

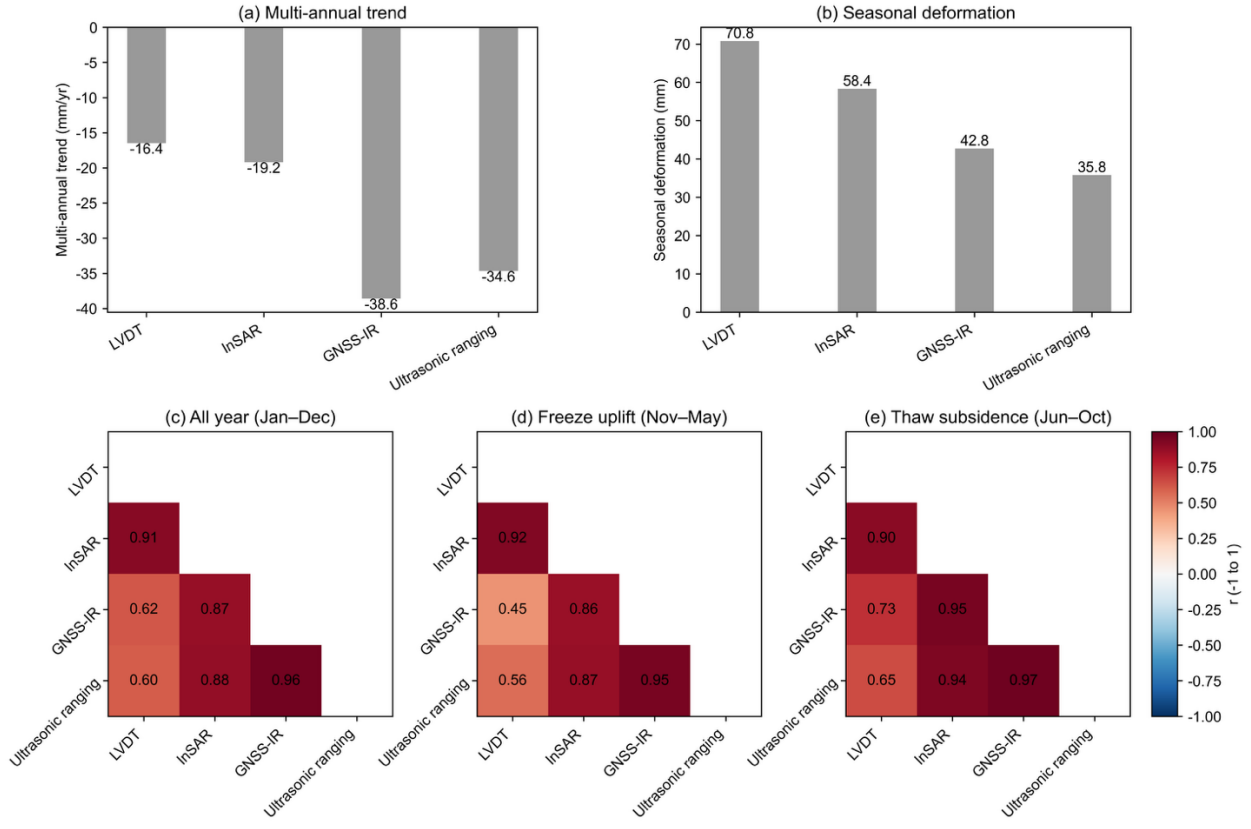

Figure 8. Intercomparison of multi-sensor deformation records. (a) Multi-annual subsidence trend and (b) seasonal deformation derived from LVDT, Sentinel-1 InSAR, GNSS-IR, and ultrasonic ranging at SLC03 supersite. (c-e) Pairwise correlation coefficients among the four deformation records for (c) the full period, (d) freeze uplift period (November–May), and (e) thaw subsidence period (June–October).

4.3 Sub-daily ground surface deformation processes based on LVDT measurements

Based on the LVDT measurements, six representative 5-day windows were selected to illustrate sub-daily deformation processes during different freeze–thaw stages (Figure 9). For each illustrated 5-day period, the deformation time series at 5 min intervals are shown together with concurrent soil temperature and soil moisture profiles recorded at 10 min intervals.

https://doi.org/10.5194/egusphere-2026-2170
Preprint. Discussion started: 19 June 2026

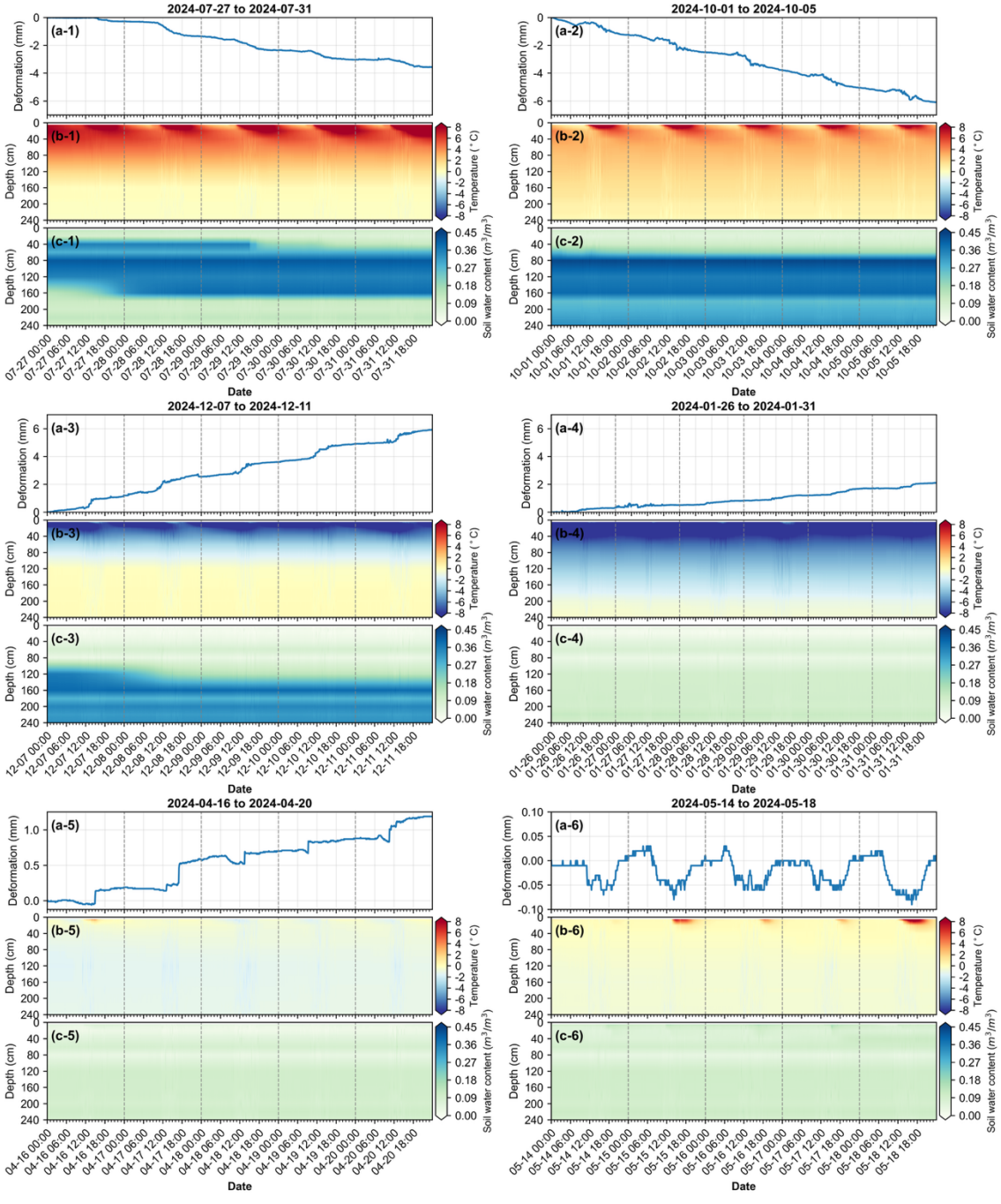

Figure 9. Representative sub-daily ground surface deformation, together with the corresponding soil temperature and moisture profiles, during different freeze–thaw stages. Panels a present ground surface deformation at 5 min resolution, with the time series

https://doi.org/10.5194/egusphere-2026-2170
Preprint. Discussion started: 19 June 2026

shifted so that the value at the first time step is zero. Panels b and c show soil temperature and soil moisture profiles, respectively, at 10 min resolution.

4.3.1 Active layer thawing with stepwise settlement (20240727–20240731)

During 27–31 July 2024, the ground surface subsided by 3.6 mm (Figure 9a-1). At 5 cm depth, soil temperature was about 2 °C at night, began rising after 08:00, and exceeded 12 °C by 17:00. The deformation is expressed as stepwise downward motion, and most settlement occurred during daytime, mainly between about 10:30 and 20:30. Outside this period, ground surface displacement was small. At 120 cm depth, soil moisture remained stable at about 0.35 m^3/m^3 and temperature at about 1.7 °C; at 180 cm depth, soil moisture remained near 0.12 m^3/m^3 and temperature near 0.1 °C. Meanwhile, soil moisture at 160 cm increased from about 0.14 m^3/m^3 on 27 July to about 0.385 m^3/m^3 on 28 July and then stay high. The hydrothermal profiles indicate that the active layer above ~160 cm was already fully thawed, while thaw progression and associated thaw settlement continued in deeper layers. Overall, this period is characterized by active layer thawing accompanied by downward migration of the thaw front and progressive settlement.

4.3.2 Late-thaw-season continuous subsidence (20241001–20241005)

From 1 to 5 October 2024, the surface subsided more rapidly than in late July, with cumulative deformation reaching 6.1 mm over only 5 d (Figure 9a–2). At this stage, the active layer above 240 cm was already fully thawed. Soil moisture at 220 cm remained near 0.30 m^3/m^3 and temperature near 0.6 °C, while at 240 cm moisture remained near 0.33 m^3/m^3 and temperature near 0.3 °C. In contrast to the stepwise settlement observed in active layer thaw period, the ground surface showed persistent subsidence throughout the day, with a weak daytime oscillation superimposed between about 08:00 and 19:00. This interval therefore represents a late-thaw-season deformation regime characterized by continuous subsidence.

4.3.3 Stepwise uplift during freeze-back (20241206–20241210)

During 6–10 December 2024, the surface underwent uplift of 6.4 mm (Figure 9a-3). The heave developed in a stepwise manner, with several distinct upward increments separated by short quasi-stable intervals. Most of the uplift occurred between about 11:00 and 15:00, whereas outside this period the uplift rate was much smaller. At 5 cm depth, temperature reached a daily maximum of about -5 °C around 16:00 and a minimum of about -15 °C around 10:00. At 60 cm depth, the daily minimum occurred around 15:00, and below 60 cm diurnal variability was weak. Soil temperatures remained below 0 °C throughout the upper 0–100 cm. At 120 cm depth, soil moisture decreased from about 0.36 m^3/m^3 on 7 October to about 0.15 m^3/m^3 on 8 October, indicating that this depth froze during the period. This stage is characterized by active layer freeze back and associated stepwise heave.

https://doi.org/10.5194/egusphere-2026-2170
Preprint. Discussion started: 19 June 2026

4.3.4 Late-winter slow uplift (20240126–20240131)

In late winter, from 30 January to 3 February 2025, the ground surface continued to heave, but much more slowly, with cumulative uplift of only 2.1 mm over 5 d (Figure 9a-4). Compared with early December, the deformation was smoother and less stepwise. Soil temperatures in the shallow layer ranged from about -6 to -15 °C, and the entire 0–240 cm profile is frozen, with liquid water content below 0.12 m^3/m^3 throughout the 240 cm profile and temperatures below 0 °C. During this period, the freezing index increased more slowly, consistent with slower freezing-front advance and weaker frost heave.

4.3.5 Early-spring heave event (20240416–20240420)

From 16 to 20 April 2024, the surface showed only a small net uplift, on the order of 1.2 mm, but the deformation developed through a sequence of discrete upward steps rather than as a continuous trend (Figure 9a-5). On 16 April, uplift occurred around 15:00 and increased by ~0.2 mm within half an hour. On 17 April, another uplift of ~0.35 mm occurred around 17:00 within half an hour. During 18–20 April, a small drop of about 0.1 mm occurred after morning warming, followed by rapid but small uplifts later in the day. At 5 cm depth, the surface layer experienced daily freeze-thaw cycling. On 16 April, the minimum temperature of about -1.6 °C occurred around 08:00 and the maximum of about 3.5 °C around 15:00. On 17 April, the temperature remained nearly constant at about −0.1 °C, and no diurnal cycle was evident, likely due to the buffering effect of latent heat released during freezing. From 18 April onward, a diurnal cycle reappeared, with maximum temperatures above 0 °C and minima near -2 °C. This process is more clearly illustrated in Appendix Figure A3c. The absence of a clear diurnal thermal cycle at 5 cm on 17 April coincided with the strongest uplift event and, together with the contemporaneous snow signal in the ultrasonic ranging record, indicates a snowmelt or rainfall infiltration event followed by rapid refreezing in the shallow soil.

4.3.6 Early-thaw season diurnal deformation (20240514–20240518)

Between 14 and 18 May 2024, the deformation was dominated by clear diurnal oscillations with an amplitude of only about ~0.05 mm and almost no cumulative net displacement over the 5 d period (Figure 9a-6). Surface deformation typically reached a daily minimum around 17:00 and a maximum around 07:00. The repeated daily uplift and settlement produced a regular wave-like pattern distinct from the monotonic heave or subsidence seen in the other windows. It is also noteworthy that diurnal deformation was enhanced on the warmest day, 18 May, when the minimum deformation was lower than on the other days. The soil temperature profile showed a pronounced shallow diurnal thermal cycle confined to the uppermost layers. Diurnal freeze-thaw cycle occurred above about 20 cm depth, while soil below 20 cm remained frozen and liquid water content remained below 0.11 m^3/m^3. At 5 cm depth, temperature reached maxima up to 10 °C and minima near -0.5 °C, whereas moisture remained relatively low, at about 0.10–0.16 m^3/m^3. This low shallow water content helps explain the very small deformation amplitude despite strong daily temperature oscillations.

https://doi.org/10.5194/egusphere-2026-2170
Preprint. Discussion started: 19 June 2026

4.4 Ground surface deformation processes and mechanisms

4.4.1 Deformation characteristics across freeze-thaw stages based on the LVDT measurements

Based on the LVDT measurements, we partitioned the deformation into the four freeze–thaw stages defined in Table 2 and illustrated in Figure 10a. Stage AT accounts for the largest negative displacement, with settlement ranging from approximately 31 to 72 mm, whereas stage LT contributes an additional 7 to >24 mm of settlement (Figure 10a). Likewise, stage AF produces most of the uplift, with heave of about 58–62 mm, while stage LF contributes a smaller additional uplift of about 6–12 mm.

Figure 10b shows the changes in the integrated active layer water content during freeze-thaw cycles. Water content decreases from September to next March and increases from March to September. The seasonal deformation magnitude and the active layer water content change are strongly proportional. A rough calculation based on the change in active layer water content multiplied by ALT indicates that ice-water phase change within the active layer can explain more than 78 % of the observed seasonal deformation.

Figure 10c–j show thaw settlement during the four thaw seasons. The onset of significant thaw settlement differs among years and, in some years, lags the onset of surface thaw. For example, major settlement began on 17 June 2023 and 2 June 2024, corresponding to lags of about 20 days and 14 days, respectively, relative to onset of AT stage. In all four years, deformation decreased progressively with thawing degree days and with thaw front deepening estimated from the Stefan equation.

The relationship between deformation and $\sqrt{\mathrm{TDD}}$ is strong, with R^2 = 0.956–0.988 (Figure 10d, 10f, 10h, 10j), indicating that thaw progression exerts a first-order control on settlement during the main thaw stage. However, the proportionality differs among years, with slopes ranging from -2.70 to -3.71 mm per $\sqrt{°\mathrm{C} \cdot \mathrm{d}}$. Among the four thaw seasons, year 2023 shows the steepest proportionality, which means the highest apparent settlement efficiency relative to cumulative thawing. Notably, in Figure 10d, 10f, 10h, 10j, the relationship between $\sqrt{\mathrm{TDD}}$ and thaw subsidence was evaluated only for the period during which thawing degree days continued to accumulate. Once thawing degree days ceased to increase, the $\sqrt{\mathrm{TDD}}$–subsidence relationship was no longer applicable. However, ground subsidence continued during this late-thaw period, and in some years this additional subsidence was substantial. This late-thaw-stage component was excluded from the correlation analysis.

https://doi.org/10.5194/egusphere-2026-2170
Preprint. Discussion started: 19 June 2026

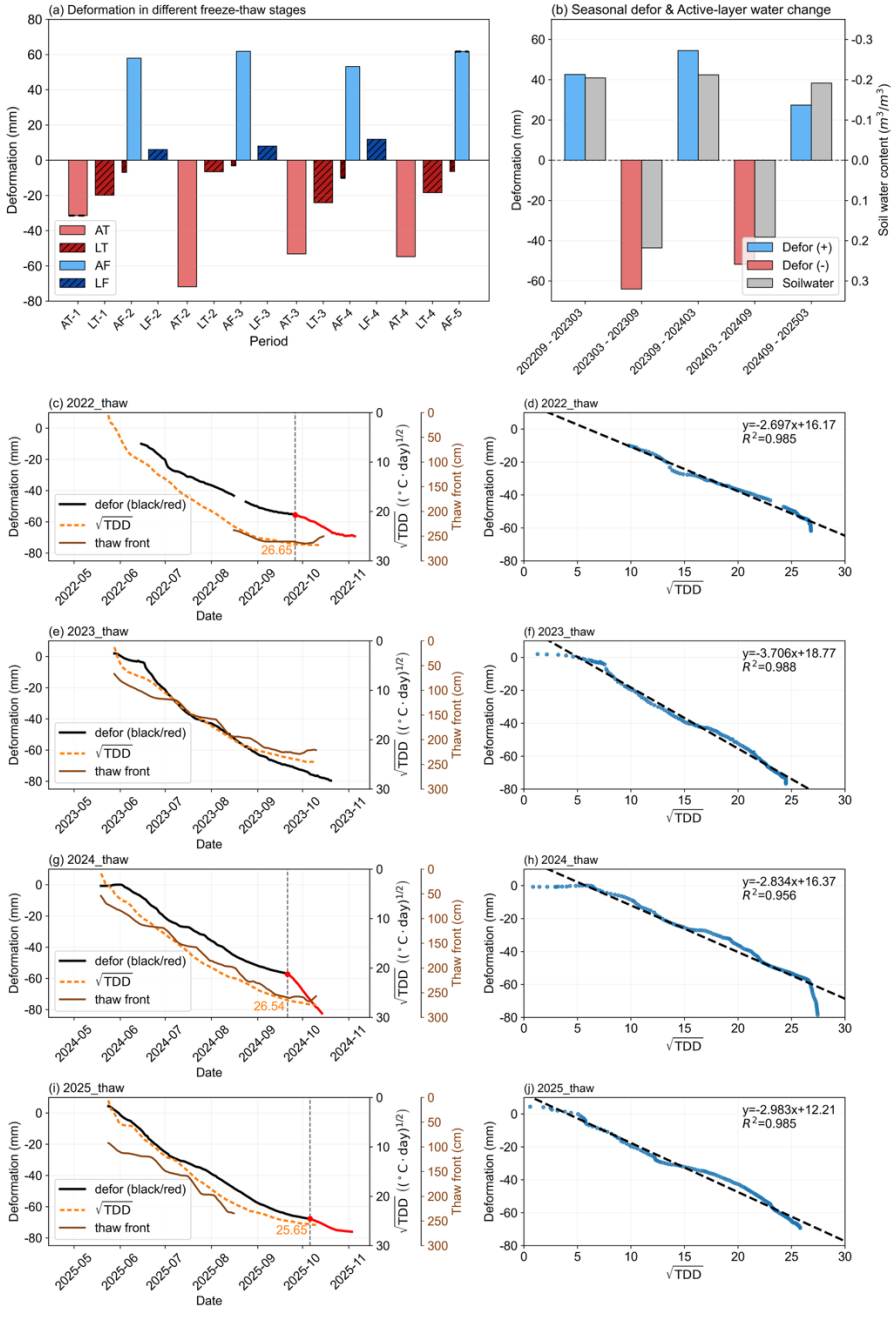

Figure 10. Deformation characteristics across freeze-thaw stages and their relationships with thaw progression. (a) Deformation partitioned into active thaw (AT), late thaw (LT), active freezing (AF), and late freezing (LF) stages for different annual cycles. (b) Seasonal deformation and active-layer water content change. (c, e, g, i) Deformation curves, $\sqrt{TDD}$, and thaw-front depth during the thaw seasons of 2022, 2023, 2024, and 2025. For ease of intercomparison, the deformation time series was shifted such that the deformation was approximately zero at $\sqrt{TDD}$ = 5. Black and red segments indicate deformation before and after the late-season

https://doi.org/10.5194/egusphere-2026-2170
Preprint. Discussion started: 19 June 2026

breakpoint, respectively. (d, f, h, j) Relationships between thaw-season deformation and $\sqrt{TDD}$ for the corresponding years, together with linear regressions.

4.4.2 Late-thaw-season subsidence and indicators of ground ice melt

Late-thaw-season subsidence at SLC03 showed strong interannual variability in both magnitude and temporal structure. In 2022, 2024, and 2025, the thaw-season deformation trajectories exhibited a distinct late-season acceleration, marked by a breakpoint after which subsidence became faster than during the preceding thaw stage (Figure 10c, 10g, 10i). The breakpoints occurred on 26 September 2022, 21 September 2024, and 6 October 2025, respectively. The cumulative settlement after the breakpoint was 13.62 mm in 2022, > 25.14 mm in 2024, and 8.37 mm in 2025. By contrast, the 2023 trajectory showed a more continuous subsidence pattern without a clear breakpoint (Figure 10e). According to the air temperature record, thawing degree days decreased in the order 2024 (752.3 °C d) > 2022 (718.5 °C d) > 2025 (665.4 °C d) > 2023 (598.8 °C d) (Figure 7d). The absence of a breakpoint in 2023 is consistent with the cooler summer conditions and reduced thaw penetration that year. Extrapolation of the temperature profile suggests a maximum thaw depth of only about 230 cm, far shallower than in the other years.

Figure 11 shows ground deformation and deep hydrothermal profiles from 11 September to 4 October 2024, spanning the period during which the acceleration breakpoint occurred. The breakpoint occurred around 21 September 2024. Before the breakpoint, thaw settlement had already slowed substantially, whereas after the breakpoint, subsidence accelerated again. During this transition, soil moisture at 240 cm increased sharply, from about 0.11 m^3/m^3 on 21 September to about 0.33 m^3/m^3 on 27 September. After the breakpoint, the sub-daily deformation trajectory differed clearly from the stepwise settlement observed during active-layer thaw: subsidence became more continuous and sustained, without the stair-step structure seen during the earlier thaw stage, as shown by comparison with Figure 9a-1 and 9a-2.

If thaw penetrates into deeper ice-rich soil, thaw of supersaturated material can generate excess meltwater beyond the storage capacity of the soil skeleton. As this excess water drains, ground volume decreases and the surface subsides. By contrast, thaw of undersaturated or saturated soil releases little or no excess water and therefore produces only minor settlement. As a simple volume-balance illustration, if the material below 240 cm is approximated as supersaturated and yields, upon thaw, 50 % excess water and 50 % saturated soil, then thawing 10 cm of this layer would generate ~5 cm of excess water and ~5 cm of saturated soil. This simple estimate suggests that drainage of excess ground ice meltwater could plausibly produce centimetre-scale surface lowering (Mackay, 1970). Beyond the theoretical inference, this study provides the direct observational evidence, based on detailed deformation measurements combined with soil hydrothermal observations, that excess ground ice melt and pore ice melt exhibit distinct characteristics.

https://doi.org/10.5194/egusphere-2026-2170
Preprint. Discussion started: 19 June 2026

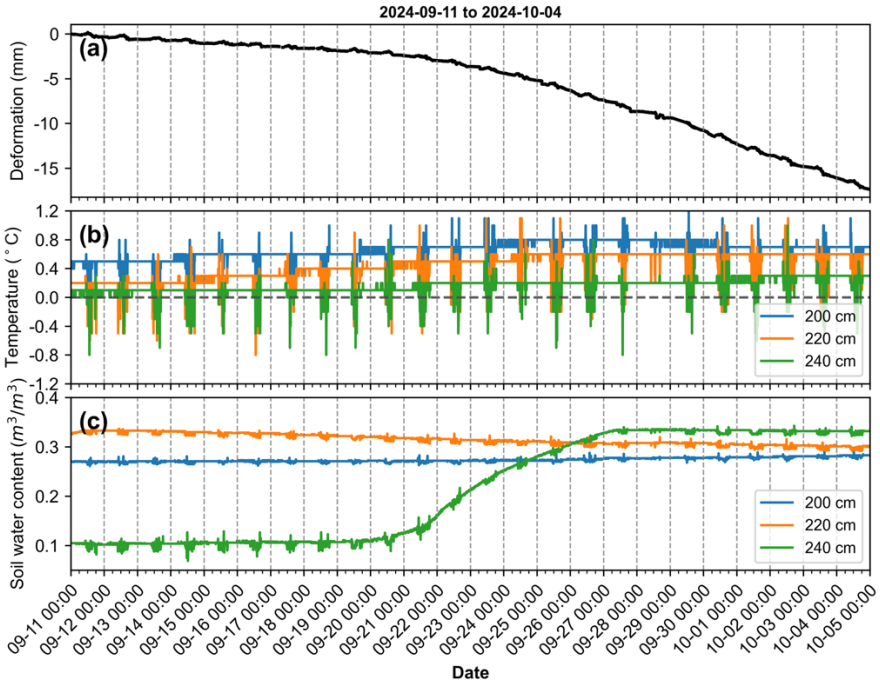

Figure 11. Late-thaw-season accelerated subsidence and associated hydrothermal profiles at the base of the active layer (200–240 cm) during 20240911–20241004. (a) Ground surface deformation recorded by the LVDT sensor at 5 min intervals. The deformation time series was shifted such that the value at the first time step was set to zero. (b, c) Soil temperature and moisture time series at 10 min intervals.

4.4.3 Late-winter slight heave and refreezing of infiltrated water

A distinct slight heave event was observed in late April to early May at both SLC03 and SLC07 Figure 4). Figure 9a-5 illustrates the detailed deformation process during 16–20 April 2024. The deformation evolved as a sequence of discrete rapid upward steps separated by short plateaus, in contrast to the smoother winter uplift observed during other periods (e.g., Figure 9a-3 and 9a-4). At SLC03, the 5 cm temperature record indicates strong freeze–thaw cycling in the shallow layer during this event. Meanwhile, the ultrasonic ranging record indicates snow accumulation followed by melt (Appendix Figure A3b). On 17 April 2024, however, the 5 cm temperature remained nearly constant at about −0.1 °C throughout the day, rather than exhibiting the usual diurnal oscillation, while uplift was also most pronounced. This suggests that latent heat released during refreezing may have damped the diurnal temperature fluctuations. Together, these observations point to snowmelt infiltration followed by rapid refreezing in the shallow soil. A similar feature was also detected at SLC07 in April 2022, where slight heave was followed by brief subsidence and then renewed slight heave before the onset of sustained thaw

https://doi.org/10.5194/egusphere-2026-2170
Preprint. Discussion started: 19 June 2026

settlement. This late-winter "dip" likely reflects the same underlying process, namely thawing and refreezing of infiltrated water.

5 Discussion

5.1 Deployment and performance of the in-situ ground surface deformation monitoring system in permafrost terrain

This study demonstrates a practical and deployable approach for high-accuracy, high-temporal-resolution continuous monitoring of permafrost ground surface deformation using an LVDT sensor–logger configuration. The system resolves elevation changes with sub-millimetre precision, capturing both sub-daily processes and multi-year deformation trends. The resulting 5-year record is, to our knowledge, among the most detailed continuous in situ deformation datasets currently available for permafrost terrain, and it confirms the robustness of the system under harsh high-altitude field conditions.

The in situ LVDT-based monitoring system resolves detailed sub-daily deformation behaviour for three main reasons. First, the sensor provides sub-millimetre precision. Second, the footplate remains in direct contact with the ground surface and is therefore largely unaffected by snow cover and vegetation. As shown in Figure 2c–d, the footplate maintains ground contact under both summer vegetation cover and winter snow cover, ensuring that the measurements represent true ground surface deformation. Third, its effective footprint is very small. In heterogeneous surface environments, observations with larger footprints integrate deformation across multiple microtopographic and subsurface settings, each characterized by different thaw and freeze onset times and different seasonal amplitudes. The superposition of these local deformation processes smooths the signal and can obscure the process-level features captured at a single point.

This study also shows that ultrasonic ranging can provide a useful complement to contact-based deformation measurements on the Tibetan Plateau. Ultrasonic ranging is sensitive to snow and vegetation and has previously been applied mainly in sparsely vegetated high-latitude environments (Overduin & Kane, 2006). In the interior Tibetan Plateau, winter snow cover is often thin, and short-lived, so snow does not permanently obscure the ground surface, thus in the ultrasonic record, snow accumulation appears as episodic positive excursions rather than as a persistent winter surface (as shown in Figure 5), and with appropriate filtering most of the underlying deformation signal can be recovered. In our study, after filtering, ultrasonic ranging shows substantial agreement with the other measurements, with correlations of 0.61 with LVDT, 0.88 with InSAR, and 0.96 with GNSS-IR. However, it should also be acknowledged that when snow cover persists beyond a certain duration, filtering cannot completely remove the snow signal, as illustrated in Figure 5 at the end of October 2022 and 2023. In such cases, the snow signal may become superimposed on the ground deformation signal and cannot be readily separated. Because substantial filtering is required to suppress distortions of vegetation and snow in ultrasonic ranging and GNSS-IR measurements, short-term deformation signals at sub-daily to sub-weekly timescales are much less reliable than those from

https://doi.org/10.5194/egusphere-2026-2170
Preprint. Discussion started: 19 June 2026

the LVDT measurements. These two non-contact methods are therefore better suited to tracking seasonal deformation amplitude and multi-year subsidence trends than to resolving subtle short-term processes.

Benchmark stability is a prerequisite for reliable monitoring of permafrost ground surface deformation. In our deployment, this requirement was addressed by anchoring steel rods or pipes deeply into the ground (e.g., 6 m for the GNSS antenna and ultrasonic ranging sensor monuments and 30 m for the LVDT reference rod, compared with an ALT of ~2.5 m). The larger subsidence rates observed by GNSS-IR and ultrasonic ranging relative to LVDT and InSAR may reflect pronounced thaw settlement associated with installation disturbance around the GNSS antenna and ultrasonic ranging sensor monuments, as shown by the field photographs in Appendix Figure A2. However, benchmark-related effects, including frost jacking or residual instability of the shallower monument foundations, cannot be entirely excluded. Notably, the discrepancy between GNSS-IR/ultrasonic ranging and LVDT/InSAR became more pronounced toward the end of the observation period, suggesting that such benchmark-related effects may have increased over time. These potential effects should therefore be carefully considered when establishing long-term monitoring systems.

Despite the successful implementation of this supersite, an important limitation remains the incomplete hydrothermal monitoring near the base of the active layer and the top of permafrost, aggravated by failure of the deepest sensors. This restricts direct characterization of deep active layer and upper-permafrost processes during probable ground ice melt events. Future systems would benefit from more reliable full-profile hydrothermal measurements spanning the active layer and the uppermost permafrost.

5.2 Significance of sub-daily deformation observations for process interpretation

The 5-min deformation record captures sub-daily ground surface processes across different freeze–thaw stages in unprecedented detail and, when interpreted together with soil temperature and moisture observations, provides direct observational support for process attribution. A first example is the origin of short-lived late-winter heave events before the main thaw-settlement stage. Similar events, including late-winter/early-spring heave followed by brief subsidence, have been detected previously and have been attributed to several possible mechanisms, including infiltration and refreezing of water in permeable frozen ground, shallow ice segregation, and phase changes near the base of the active layer (Gruber, 2020; Harris et al., 2008; Matsumoto et al., 2010; Matsuoka et al., 1997). At SLC03, the deformation process during 16–20 April, 2024 (Figure 9a-5) consists of several discrete upward steps separated by short plateaus. The sub-daily deformation record, combined with soil temperature and moisture profiles and snow information, provides direct support for the interpretation that such late-winter heave is more plausibly attributed to infiltration and rapid refreezing in shallow soil than to continuous formation of shallow segregation ice.

https://doi.org/10.5194/egusphere-2026-2170
Preprint. Discussion started: 19 June 2026

A second example is the acceleration of subsidence late in the thaw season. The 5-min deformation record shows that deformation associated with thaw within the active layer differs systematically from that associated with late-season deep thaw. During active layer thaw, settlement is commonly stepwise, whereas after the late-season breakpoint settlement becomes more continuous. This contrast indicates that the accelerated late-season subsidence reflects a different deformation regime, consistent with continued drainage and compression following excess ground ice melt.

A third contribution is that the sub-daily record clarifies the form of diurnal frost-heave deformation. Although the daily freeze–thaw cycles at the SLC03 site had amplitudes of less than 1 mm, the pattern of heave and subsidence closely resembled that of the seasonal deformation cycle. Earlier studies from the Canadian and Colorado Rockies have shown that diurnal freeze–thaw deformation is predominantly a near-surface process (Fahey, 1973; Smith, 1987), generally confined to the upper 10 cm of soil, with typical vertical displacements of only a few millimetres; accordingly, its geomorphic significance is thought to be largely limited to micro-scale surface disturbance rather than the development of large-scale periglacial landforms. At the SLC03 site, the mean soil moisture at 5 cm depth during July–August was only 0.116 m^3/m^3. The relatively coarse soil texture and low soil moisture content likely constrained the magnitude of diurnal freeze–thaw deformation. Nevertheless, even such small-amplitude deformation can still be resolved and interpreted, providing useful information on near-surface thermal and hydrological conditions.

5.3 Controls on the spatiotemporal variability of ground surface deformation

Ground surface deformation varied strongly both between sites and among years. In this study, SLC03 and SLC07, although only 25 km apart, show marked differences in seasonal deformation amplitude, in the onset timing of thaw settlement and freeze-back heave, and in overall process shape (Figure 4); the correlation coefficient between the two LVDT records from the two sites (SLC03 and SLC07) is only 0.61. Interannual variability was also substantial at each site. At SLC07, both frost heave and thaw subsidence were substantially greater following a wetter year, indicating a strong influence of soil water content on seasonal deformation. Meanwhile, the annual maximum deformation did not decline monotonically, whereas the seasonal minima showed net subsidence. This suggests that when observation periods are short, trends inferred from seasonal minima or maxima alone may be misleading. The timing of thaw-settlement onset also varied among years. At SLC03, rapid settlement began more than two weeks after the onset of the AT stage in some years. The coarse-textured and relatively dry near-surface soil at SLC03 (summer mean soil moisture of ~0.116 m^3/m^3 at 5 cm depth; Figure 7c) likely contains abundant macropores, such that shallow thaw can occur without generating pronounced immediate settlement. This indicates that not all thawing events necessarily produce substantial deformation, particularly in relatively dry or coarse-textured soils. Despite variability in timing, active-layer thaw settlement at SLC03 remained closely linked to thaw progression, with the underlying mechanism being the phase transition amount from ice to water within the thawed layer. Across all four thaw seasons, settlement during the main thaw stage exhibited a strong correlation with $\sqrt{\mathrm{TDD}}$, although the

https://doi.org/10.5194/egusphere-2026-2170
Preprint. Discussion started: 19 June 2026

proportionality varied among years (2.7–3.7 mm per $\sqrt{°C \cdot d}$; Figure 10d, 10f, 10h, 10j). An interesting feature is that settlement efficiency was the highest in 2023, not in the warmer years 2022 or 2024. At SLC03, substantial settlement occurred in 2023 despite relatively low ADDT and a thaw depth of only ~236 cm. This suggests that the mechanical response of the thawed layer was also modulated by antecedent hydrothermal and structural conditions. Following an exceptionally warm year of 2022, redistribution of meltwater and subsurface structural adjustment may have increased the susceptibility of the ground to compression and thaw consolidation in the following year.

At both SLC03 and SLC07, the LVDT records showed little evidence of short-term hydrologically driven deformation features, such as precipitation-induced deformation, wetting-related swelling of fine-grained soils, and drainage-triggered elevation changes (Gruber, 2020). Previous studies have also suggested that heavy rainfall can introduce short-term perturbations into InSAR-derived deformation signals (Wang et al., 2020). By comparison, the deformation series at both of our sites are comparatively "clean", with weak short-term fluctuations. This likely reflects the relatively dry, coarse-textured surface soil and thin organic layer, which damp shallow hydrological perturbations. Comparisons between our sites and others therefore suggest that near-surface soil texture and organic-layer thickness exert important controls on whether deformation time series in permafrost terrain are smooth or, conversely, dominated by event-like variability.

5.4 Deformation-based indicators of excess ground ice melt

Recent InSAR-based studies in Alaska and in Svalbard showed that late-season subsidence during exceptionally warm summers was much greater in ice-rich than in ice-poor terrain (Wendt et al., 2026; Zwieback & Meyer, 2021) and suggested that such subsidence could be used to identify ice-rich permafrost and infer excess ground ice content (Zwieback et al., 2025; Zwieback, Iwahana, et al., 2024). Our observations support this idea and show that late-season subsidence provides a useful process-based indicator of deep thaw and excess ground ice melt.

When thaw reaches ice-supersaturated material near the top of permafrost, excess meltwater is generated and subsequent drainage and thaw consolidation lead to enhanced surface lowering. In contrast, thaw of ice-undersaturated or merely saturated soil produces little excess water and therefore little additional settlement. In this context, a late-season breakpoint-style acceleration in subsidence is best interpreted as a process-specific signature of thaw engaging ice-rich permafrost. In our record, such breakpoint-style acceleration is evident in year 2022 (20220926), 2024 (20240921), and 2025 (20251006), but not in 2023. The presence, timing, and magnitude of the breakpoint depend on heat accumulation, the vertical distribution of ground ice, and local drainage conditions, all of which can sharpen or smooth the deformation response.

If excess ground ice is limited in abundance, or if the contrast in ice content between layers is small, the acceleration signal can be weak relative to measurement noise and can be obscured by spatial averaging. This is evident at SLC03, where the LVDT record shows a clear late-thaw-season acceleration, whereas the corresponding feature is much less distinct in GNSS-

https://doi.org/10.5194/egusphere-2026-2170
Preprint. Discussion started: 19 June 2026

IR, ultrasonic ranging, and InSAR. In some locations, seasonal deformation may vary greatly among years, and late-season acceleration may not be clearly expressed, as at site SLC07. Under such conditions, the multiannual subsidence trend may provide a more robust outcome indicator of the cumulative deformation legacy of ground ice loss. Both indicators are informative at the regional scale. In the Arctic, retrieving multiannual continuous deformation is often challenging because snow cover in winter and wet snow during spring snowmelt can cause strong decorrelation. In such cases, thaw-season deformation, along with interannual comparisons of thaw-season deformation processes, may still provide valuable information on ground ice melt.

6 Conclusion

Using collocated in situ LVDT-based monitoring, ultrasonic ranging, GNSS-IR, Sentinel-1 SBAS-InSAR, and multi-depth hydrothermal observations at a permafrost supersite on the central Tibetan Plateau, this study analysed ground surface deformation from sub-daily to multi-year timescales and related it to different freeze–thaw processes. The main conclusions are as follows.

(1) A practical and robust in situ LVDT-based displacement monitoring system was established for high-temporal-resolution, high-precision monitoring of permafrost ground surface deformation. Owing to direct footplate–ground contact, the system is largely unaffected by snow cover and vegetation, and it provides continuous measurements at 5 min intervals with sub-millimetre precision and stable long-term performance under harsh plateau conditions.

(2) Sub-daily deformation processes were resolved for the first time across different freeze–thaw stages. The 5-min step continuous record revealed distinct deformation behaviours during active-layer thaw, excess ground ice melt, active layer freezing, late-winter freezing, and early thaw-season diurnal cycling. Settlement during active-layer thaw commonly occurred in a stepwise manner, whereas settlement by excess ground ice melting was more continuous, implying sustained drainage and consolidation following excess ground ice melt. The slight heave observed in late winter, prior to the main thaw-settlement stage, is best explained by the infiltration and rapid refreezing of liquid water in the shallow soil. The early thaw-season diurnal cycle resembled the seasonal deformation pattern, but its magnitude was much smaller.

(3) The collocated multi-sensor observations provide a critical benchmark for evaluating the strengths and limitations of LVDT, GNSS-IR, ultrasonic ranging, and InSAR, and lay the foundation for integrated monitoring of permafrost deformation dynamics. The four deformation monitoring results exhibit broadly consistent patterns. Among them, LVDT and InSAR are more similar to each other ($r = 0.91$), while GNSS-IR and ultrasonic ranging show even closer agreement ($r = 0.96$). The relatively low-snow conditions on the Tibetan Plateau enable GNSS-IR and ultrasonic ranging to provide useful seasonal and long-term deformation measurement. However, detailed deformation processes are more reliably resolved by the LVDT-based measurements.

(4) Ground surface deformation exhibited marked spatiotemporal heterogeneity, with substantial differences between nearby sites and among years in seasonal deformation amplitude, timing, and long-term trends. In relatively dry soils with low

https://doi.org/10.5194/egusphere-2026-2170
Preprint. Discussion started: 19 June 2026

organic matter content, the deformation signal was less influenced by hydrological events. At SLC03, active-layer thaw subsidence was closely proportional to $\sqrt{TDD}$, and seasonal deformation was primarily governed by the amount of phase-change water in the active layer, which explained more than 78% of the observed seasonal deformation.

(5) The late-thaw-season acceleration in subsidence serves as a process-based indicator of ice-rich permafrost thaw and subsequent drainage and consolidation, whereas multi-year subsidence trend reflects the cumulative outcome of these processes.

Overall, this study provides a valuable field-based benchmark of permafrost deformation from sub-daily to multi-year timescales, improves understanding of freeze–thaw deformation processes, and offers observational reference for process-based modelling and for interpretation and validation of remote-sensing observations in permafrost regions.

Data availability

The Sentinel-1 Level-1 Single Look Complex (SLC) images analysed in this study are openly available from the Alaska Satellite Facility (ASF) Distributed Active Archive Center at https://search.asf.alaska.edu/.

Author contributions

Lingxiao Wang: Conceptualization, Methodology, Data curation, Formal analysis, Investigation, Visualization, Funding acquisition, Writing – original draft. Wei Wan: Methodology, Formal analysis, Resources, Funding acquisition, Writing – review & editing. Lin Zhao: Methodology, Resources, Funding acquisition, Writing – review & editing. Wei Chen: Data curation, Visualization, Formal analysis. Chong Wang: Data curation, Investigation, Project administration, Writing – review & editing. Shibo Liu: Methodology, Data curation, Investigation. Guangyue Liu: Methodology, Data curation, Investigation, Project administration. Yuanwei Wang: Data curation, Investigation. Junhao Qu: Formal analysis, Visualization. Defu Zou: Methodology, Data curation, Investigation. Erji Du: Data curation, Investigation. Guojie Hu: Formal analysis. Yao Xiao: Formal analysis. Yonghua Zhao: Data curation. Minxuan Xiao: Investigation.

Competing interests

The authors declare that they have no competing interests.

Acknowledgements

We thank Kan Zhang of Beijing Truwel Instruments, Inc., Chengye Li of Nanjing University of Information Science and Technology, and Huayun Zhou of the Northwest Institute of Eco-Environment and Resources for their valuable assistance with field deployment and instrument installation.

https://doi.org/10.5194/egusphere-2026-2170
Preprint. Discussion started: 19 June 2026

Financial support

This research was supported by the National Natural Science Foundation of China (Grant No. 42376254 & No. 42471511), the Second Tibetan Plateau Scientific Expedition and Research (STEP) program (Grant No. 2019QZKK0201), the Natural Science Foundation of the Jiangsu Province (Grant No. BK20251887), and the Beijing Nova Program (Grant No. 20230484327).

Appendix

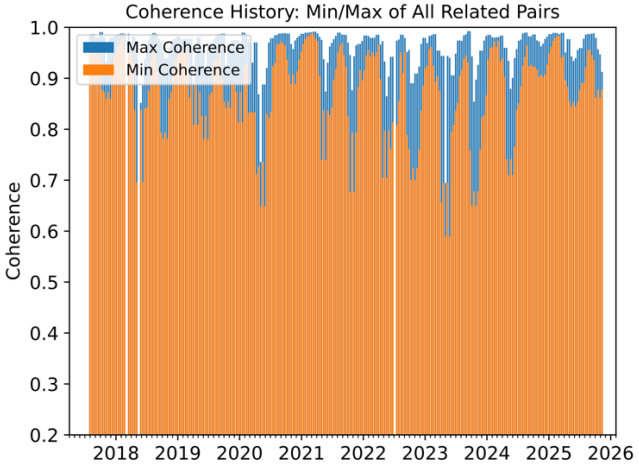

Figure A1. Overview of interferometric coherence: the minimum and maximum mean coherence of all interferogram pairs associated with each acquisition date.

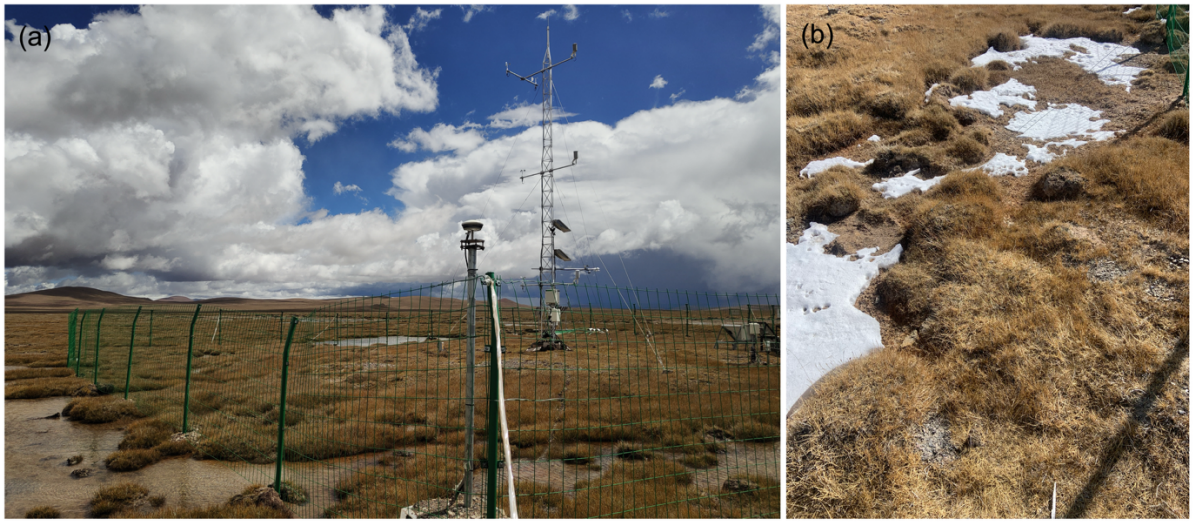

Figure A2. Field photographs showing (a) summer conditions, with several thermokarst ponds developed near the GNSS antenna and the steel meteorological tower, and (b) winter conditions, with evident ground subsidence near the GNSS antenna monument.

https://doi.org/10.5194/egusphere-2026-2170
Preprint. Discussion started: 19 June 2026

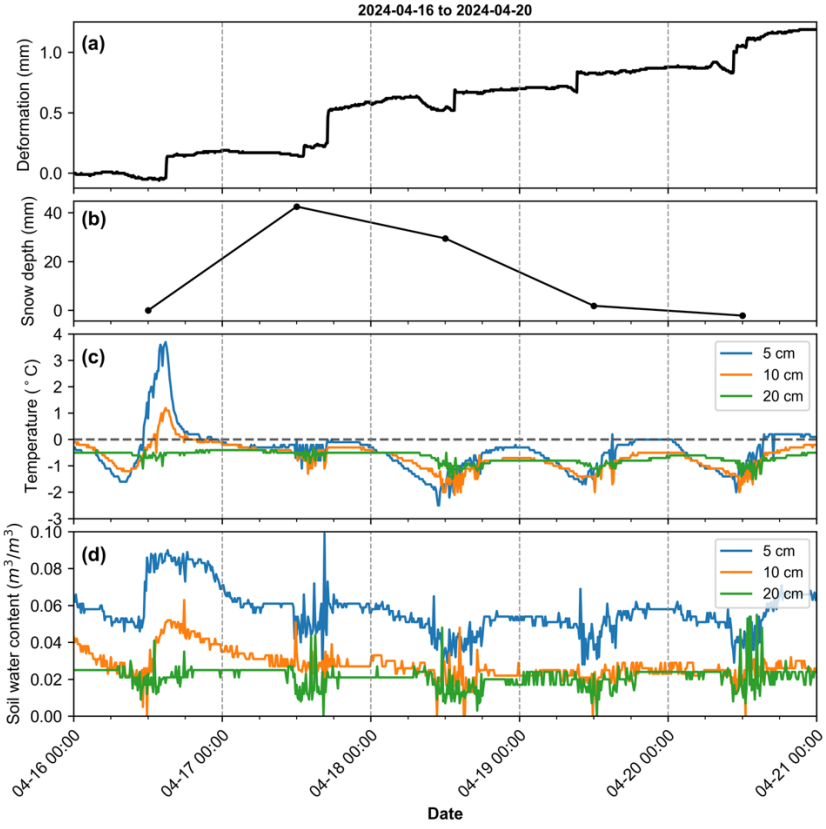

Figure A3. Sub-daily ground surface deformation and concurrent soil temperature and moisture profiles at 5–20 cm depth during 16–20 April 2024. Snow depth was derived from daily raw ultrasonic ranging data and is presented relative to the first day, with the first-day value shifted to zero.

References

Aga, J., Boike, J., Langer, M., Ingeman-Nielsen, T., & Westermann, S. (2023). Simulating ice segregation and thaw consolidation in permafrost environments with the CryoGrid community model. *The Cryosphere*, *17*(10), 4179–4206. https://doi.org/10.5194/tc-17-4179-2023

Antonova, S., Sudhaus, H., Strozzi, T., Zwieback, S., Kääb, A., Heim, B., Langer, M., Bornemann, N., & Boike, J. (2018). Thaw Subsidence of a Yedoma Landscape in Northern Siberia, Measured In Situ and Estimated from TerraSAR-X Interferometry. *Remote Sensing*, *10*(4), 494.

Chen, C. W., & Zebker, H. A. (2002). Phase unwrapping for large SAR interferograms: Statistical segmentation and generalized network models. *IEEE Transactions on Geoscience and Remote Sensing*, *40*(8), 1709–1719.

Chen, J., Wu, Y., O'Connor, M., Cardenas, M. B., Schaefer, K., Michaelides, R., & Kling, G. (2020). Active layer freeze-thaw and water storage dynamics in permafrost environments inferred from InSAR. *Remote Sensing of Environment*, *248*, 112007.

https://doi.org/10.5194/egusphere-2026-2170
Preprint. Discussion started: 19 June 2026

Chen, W., Wang, L., Zhao, L., Wan, W., Liu, S., Wang, C., Zhao, L., Liu, G., Zou, D., Liang, C., Wang, Y., & Huang, C. (2025). Details and Mechanisms of Permafrost Ground Deformation on the Tibetan Plateau Revealed by GNSS-IR and In Situ Hydrothermal Monitoring. *Journal of Geophysical Research: Earth Surface*, *130*(5), e2024JF008012. https://doi.org/10.1029/2024JF008012

Du, E., Wang, L., Zhao, L., Zhou, H., Liu, S., Zou, D., Liu, G., Xiao, Y., Hu, G., Li, Z., & others. (2025). Quantifying the soil water content of the permafrost active layer using InSAR deformation. *Journal of Hydrology*, 133660.

Fahey, B. D. (1973). An Analysis of Diurnal Freeze-Thaw and Frost Heave Cycles in the Indian Peake Region of the Colorado Front Range. *Arctic and Alpine Research*, *5*(3), 269. https://doi.org/10.2307/1550034

Fan, C., Mu, C., Liu, L., Zhang, T., Jia, S., Wang, S., Sun, W., & Zhao, Z. (2025). Time-Series models for ground subsidence and heave over permafrost in InSAR Processing: A comprehensive assessment and new improvement. *ISPRS Journal of Photogrammetry and Remote Sensing*, *222*, 167–185. https://doi.org/10.1016/j.isprsjprs.2025.02.019

Gruber, S. (2020). Ground subsidence and heave over permafrost: Hourly time series reveal interannual, seasonal and shorter-term movement caused by freezing, thawing and water movement. *The Cryosphere*, *14*(4), 1437–1447.

Harris, C., Kern-Luetschg, M., Smith, F., & Isaksen, K. (2008). Solifluction processes in an area of seasonal ground freezing, Dovrefjell, Norway. *Permafrost and Periglacial Processes*, *19*(1), 31–47. https://doi.org/10.1002/ppp.609

Harris, C., Luetschg, M., Davies, M. C., Smith, F., Christiansen, H. H., & Isaksen, K. (2007). Field instrumentation for real-time monitoring of periglacial solifluction. *Permafrost and Periglacial Processes*, *18*(1), 105–114.

Hjort, J., Streletskiy, D., Doré, G., Wu, Q., Bjella, K., & Luoto, M. (2022). Impacts of permafrost degradation on infrastructure. *Nature Reviews Earth & Environment*, *3*(1), 24–38. https://doi.org/10.1038/s43017-021-00247-8

Hu, Y., Wang, J., Li, Z., & Peng, J. (2022). Ground surface elevation changes over permafrost areas revealed by multiple GNSS interferometric reflectometry. *Journal of Geodesy*, *96*(8), 56. https://doi.org/10.1007/s00190-022-01646-5

Kokelj, S. V., Burn, C. R., & Tarnocai, C. (2007). The Structure and Dynamics of Earth Hummocks in the Subarctic Forest Near Inuvik, Northwest Territories, Canada. *Arctic, Antarctic, and Alpine Research*, *39*(1), 99–109.

Kokelj, S. V., Kokoszka, J., van Der Sluijs, J., Rudy, A. C., Tunnicliffe, J., Shakil, S., Tank, S. E., & Zolkos, S. (2021). Thaw-driven mass wasting couples slopes with downstream systems, and effects propagate through Arctic drainage networks. *The Cryosphere*, *15*(7), 3059–3081.

Larson, K. M., & Nievinski, F. G. (2013). GPS snow sensing: Results from the EarthScope Plate Boundary Observatory. *GPS Solutions*, *17*(1), 41–52. https://doi.org/10.1007/s10291-012-0259-7

Little, J. D., Sandall, H., Walegur, M. T., & Nelson, F. E. (2003). Application of differential global positioning systems to monitor frost heave and thaw settlement in tundra environments. *Permafrost and Periglacial Processes*, *14*(4), 349–357.

Liu, L., & Larson, K. M. (2018). Decadal changes of surface elevation over permafrost area estimated using reflected GPS signals. *Cryosphere*, *12*(2).

https://doi.org/10.5194/egusphere-2026-2170
Preprint. Discussion started: 19 June 2026

Liu, S., Zhao, L., Wang, L., Zhou, H., Zou, D., Sun, Z., Xie, C., & Qiao, Y. (2022). Intra-annual ground surface deformation detected by site observation, simulation and InSAR monitoring in permafrost site of Xidatan, Qinghai-Tibet Plateau. *Geophysical Research Letters*, *49*(3), e2021GL095029.

Mackay, J. R. (1970). Disturbances to the tundra and forest tundra environment of the western Arctic. *Canadian Geotechnical Journal*, *7*(4), 420–432. https://doi.org/10.1139/t70-054

Mackay, J. R., & Burn, C. R. (2002). The first 20 years (1978-1979 to 1998-1999) of active-layer development, Illisarvik experimental drained lake site, western Arctic coast, Canada. *Canadian Journal of Earth Sciences*, *39*(11), 1657–1674.

Matsumoto, H., Yamada, S., & Hirakawa, K. (2010). Relationship between ground ice and solifluction: Field measurements in the Daisetsu Mountains, northern Japan. *Permafrost and Periglacial Processes*, *21*(1), 78–89. https://doi.org/10.1002/ppp.675

Matsuoka, N., Hirakawa, K., Watanabe, T., & Moriwaki, K. (1997). Monitoring of Periglacial Slope Processes in the Swiss Alps: The First Two Years of Frost Shattering, Heave and Creep. *Permafrost and Periglacial Processes*, *8*(2), 155–177. https://doi.org/10.1002/(SICI)1099-1530(199732)8:2%253C155::AID-PPP248%253E3.0.CO;2-N

Nitzbon, J., Westermann, S., Langer, M., Martin, L. C., Strauss, J., Laboor, S., & Boike, J. (2020). Fast response of cold ice-rich permafrost in northeast Siberia to a warming climate. *Nature Communications*, *11*(1), 2201.

O'Neill, H. B., & Burn, C. R. (2012). Physical and temporal factors controlling the development of near-surface ground ice at Illisarvik, western Arctic coast, Canada. *Canadian Journal of Earth Sciences*, *49*(9), 1096–1110.

O'Neill, H. B., Smith, S. L., & Duchesne, C. (2019). *Long-term permafrost degradation and thermokarst subsidence in the Mackenzie Delta area indicated by thaw tube measurements*. 643–651.

Overduin, P. P., & Kane, D. L. (2006). Frost boils and soil ice content: Field observations. *Permafrost and Periglacial Processes*, *17*(4), 291–307. https://doi.org/10.1002/ppp.567

Shiklomanov, N. I., Streletskiy, D. A., Little, J. D., & Nelson, F. E. (2013). Isotropic thaw subsidence in undisturbed permafrost landscapes. *Geophysical Research Letters*, *40*(24), 6356–6361.

Short, N., LeBlanc, A.-M., Sladen, W., Oldenborger, G., Mathon-Dufour, V., & Brisco, B. (2014). RADARSAT-2 D-InSAR for ground displacement in permafrost terrain, validation from Iqaluit Airport, Baffin Island, Canada. *Remote Sensing of Environment*, *141*, 40–51. https://doi.org/10.1016/j.rse.2013.10.016

Smith, D. J. (1987). Frost-Heave Activity in the Mount Rae Area, Canadian Rocky Mountains. *Arctic and Alpine Research*, *19*(2), 155–166. https://doi.org/10.1080/00040851.1987.12002589

Streletskiy, D. A., Maslakov, A., Grosse, G., Shiklomanov, N. I., Farquharson, L., Zwieback, S., Iwahana, G., Bartsch, A., Liu, L., Strozzi, T., Lee, H., & Debolskiy, M. V. (2025). Thawing permafrost is subsiding in the Northern Hemisphere—Review and perspectives. *Environmental Research Letters*, *20*(1), 013006. https://doi.org/10.1088/1748-9326/ada2ff

Streletskiy, D. A., Shiklomanov, N. I., Little, J. D., Nelson, F. E., Brown, J., Nyland, K. E., & Klene, A. E. (2016). Thaw subsidence in undisturbed tundra landscapes, Barrow, Alaska, 1962–2015. *Permafrost and Periglacial Processes*, *28*(3), 566–572.

https://doi.org/10.5194/egusphere-2026-2170
Preprint. Discussion started: 19 June 2026

Tu, J., He, X., Wang, X., & Song, M. (2025). A 20-Year Monitoring of Seasonal and Long-Term Surface Elevation Changes in Permafrost Areas Using GPS Interferometric Reflectometry. *IEEE Journal of Selected Topics in Applied Earth Observations and Remote Sensing*, *18*, 26547–26560. https://doi.org/10.1109/JSTARS.2025.3621727

Wang, L., Marzahn, P., Bernier, M., & Ludwig, R. (2020). Sentinel-1 InSAR measurements of deformation over discontinuous permafrost terrain, Northern Quebec, Canada. *Remote Sensing of Environment*, *248*, 111965. https://doi.org/10.1016/j.rse.2020.111965

Wang, L., Zhao, L., Zhou, H., Liu, S., Du, E., Zou, D., Liu, G., Xiao, Y., Hu, G., Wang, C., & others. (2022). Contribution of ground ice melting to the expansion of Selin Co (lake) on the Tibetan Plateau. *The Cryosphere*, *16*(7), 2745–2767.

Wendt, L., Rouyet, L., Christiansen, H. H., Lauknes, T. R., & Westermann, S. (2026, February 16). InSAR sensitivity to active layer ground ice content in Adventdalen, Svalbard. *The Cryosphere*, *20*(2), 1179–1197. https://doi.org/doi.org/10.5194/tc-20-1179-2026

Zhang, J., Liu, L., & Hu, Y. (2020). Global Positioning System interferometric reflectometry (GPS-IR) measurements of ground surface elevation changes in permafrost areas in northern Canada. *The Cryosphere*, *14*(6), 1875–1888. https://doi.org/10.5194/tc-14-1875-2020

Zhang, J., Liu, L., Su, L., & Che, T. (2021). Three in one: GPS-IR measurements of ground surface elevation changes, soil moisture, and snow depth at a permafrost site in the northeastern Qinghai–Tibet Plateau. *The Cryosphere*, *15*(6), 3021–3033.

Zhang, Z., Lin, H., Wang, M., Liu, X., Chen, Q., Wang, C., & Zhang, H. (2022). A Review of Satellite Synthetic Aperture Radar Interferometry Applications in Permafrost Regions: Current status, challenges, and trends. *IEEE Geoscience and Remote Sensing Magazine*, *10*(3), 93–114. https://doi.org/10.1109/MGRS.2022.3170350

Zwieback, S., Iwahana, G., Chang, Q., & Meyer, F. (2025). InSAR estimates of excess ground ice concentrations near the permafrost table. *ISPRS Journal of Photogrammetry and Remote Sensing*, *223*, 261–273. https://doi.org/10.1016/j.isprsjprs.2025.03.004

Zwieback, S., Iwahana, G., Sakhalkar, S., Biessel, R., Taylor, S., & Meyer, F. J. (2024). Excess Ground Ice Profiles in Continuous Permafrost Mapped From InSAR Subsidence. *Water Resources Research*, *60*(2), e2023WR035331. https://doi.org/10.1029/2023WR035331

Zwieback, S., Liu, L., Rouyet, L., Short, N., & Strozzi, T. (2024). Advances in InSAR Analysis of Permafrost Terrain. *Permafrost and Periglacial Processes*, *35*(4), 544–556. https://doi.org/10.1002/ppp.2248

Zwieback, S., & Meyer, F. J. (2021). Top-of-permafrost ground ice indicated by remotely sensed late-season subsidence. *The Cryosphere*, *15*(4), 2041–2055.